First Year *Wilkinson Microwave Anisotropy Probe* (*WMAP*) Observations: Foreground Emission

C. L. Bennett[2], R. S. Hill[3], G. Hinshaw[2], M. R. Nolta[4], N. Odegard[3], L. Page[4], D. N. Spergel[5], J. L. Weiland[3], E. L. Wright[6], M. Halpern[7], N. Jarosik[4], A. Kogut[2], M. Limon[2,8], S. S. Meyer[9], G. S. Tucker[2,8,10], E. Wollack[2]

Charles.L.Bennett@NASA.gov

ABSTRACT

The *WMAP* mission has mapped the full sky to determine the geometry, content, and evolution of the universe. Full sky maps are made in five microwave frequency bands to separate the temperature anisotropy of the cosmic microwave background (CMB) from foreground emission, including diffuse Galactic emission and Galactic and extragalactic point sources. We define masks that excise regions of high foreground emission, so CMB analyses can be carried out with minimal foreground contamination. We also present maps and spectra of the individual emission components, leading to an improved understanding of Galactic astrophysical processes. The effectiveness of template fits to remove foreground emission from the *WMAP* data is also examined. These efforts result in a CMB map with minimal contamination and a demonstration that the *WMAP* CMB power spectrum is insensitive to residual foreground emission.

We use a Maximum Entropy Method to construct a model of the Galactic emission components. The observed total Galactic emission matches the model to <1% and the individual model components are accurate to a few percent. We find that the Milky Way resembles other normal spiral galaxies between 408 MHz and 23 GHz, with a synchrotron spectral index that is flattest ($\beta_s \sim -2.5$) near star-forming regions, especially in the plane, and steepest ($\beta_s \sim -3$) in the halo. This is consistent with a picture of relativistic cosmic ray electron generation in star-forming regions and diffusion and convection within the plane. The significant synchrotron index steepening out of the plane suggests a diffusion process in which the halo electrons are trapped in the Galactic potential long enough to suffer synchrotron and inverse Compton energy losses and hence a spectral steepening. The synchrotron index is steeper in the *WMAP*

[1] *WMAP* is the result of a partnership between Princeton University and NASA's Goddard Space Flight Center. Scientific guidance is provided by the *WMAP* Science Team.

[2] Code 685, Goddard Space Flight Center, Greenbelt, MD 20771

[3] Science Systems and Applications, Inc. (SSAI), 10210 Greenbelt Road, Suite 600 Lanham, Maryland 20706

[4] Dept. of Physics, Jadwin Hall, Princeton, NJ 08544

[5] Dept of Astrophysical Sciences, Princeton University, Princeton, NJ 08544

[6] UCLA Astronomy, PO Box 951562, Los Angeles, CA 90095-1562

[7] Dept. of Physics and Astronomy, University of British Columbia, Vancouver, BC Canada V6T 1Z1

[8] National Research Council (NRC) Fellow

[9] Depts. of Astrophysics and Physics, EFI and CfCP, University of Chicago, Chicago, IL 60637

[10] Dept. of Physics, Brown University, Providence, RI 02912

bands than in lower frequency radio surveys, with a spectral break near 20 GHz to $\beta_s < -3$. The modeled thermal dust spectral index is also steep in the *WMAP* bands, with $\beta_d \approx 2.2$. Our model is driven to these conclusions by the low level of total foreground contamination at ~ 60 GHz. Microwave and Hα measurements of the ionized gas agree well with one another at about the expected levels. Spinning dust emission is limited to $< 5\%$ of the Ka-band foreground emission.

A catalog of 208 point sources is presented. The reliability of the catalog is 98%, i.e., we expect five of the 208 sources to be statistically spurious. The mean spectral index of the point sources is $\alpha \sim 0$ ($\beta \sim -2$). Derived source counts suggest a contribution to the anisotropy power from unresolved sources of $(15.0 \pm 1.4) \times 10^{-3}\,\mu\mathrm{K}^2\mathrm{sr}$ at Q-band and negligible levels at V-band and W-band. The Sunyaev-Zeldovich effect is shown to be a negligible "contamination" to the maps.

Subject headings: cosmic microwave background, cosmology: observations, Galaxy: structure, (ISM:) cosmic rays, ISM: structure, Galaxy: general, Galaxy: halo, (cosmology:) diffuse radiation, radio continuum: ISM

1. INTRODUCTION

The *Wilkinson Microwave Anisotropy Probe* (*WMAP*)[1] mission was designed to make precise, accurate, and reliable measurements of the microwave sky to allow the extraction of cosmological information from the cosmic microwave background (CMB) radiation (Bennett et al. 2003). Use of the CMB for cosmology is limited, however, by microwave foreground contamination from our Milky Way Galaxy and from extragalactic sources.

The separation of the CMB and foreground signal components fundamentally relies on their differing spectral and spatial distributions. To facilitate the separation of signal components, *WMAP* was designed to map the full sky at five widely separated frequencies, from 23 GHz to 94 GHz (see Table 1). A similar approach was taken by the *COBE* mission (Bennett et al. 1992), although with only three frequency bands. While *COBE* resulted in a 6144 pixel map, the *WMAP* map has 3,145,728 sky pixels, with 3.995×10^{-6} sr per pixel. The *WMAP* mission is described by Bennett et al. (2003), the optical design by Page et al. (2003b), the feed horns by Barnes et al. (2002), and the radiometers and their frequency coverage by Jarosik et al. (2003).

In this paper we follow the notation convention that flux density is $S \sim \nu^{\alpha}$ and antenna temperature is $T \sim \nu^{\beta}$, where the spectral indices are related by $\beta = \alpha - 2$. In general, the CMB is expressed in terms of thermodynamic temperature, while Galactic and extragalactic foregrounds are expressed in antenna temperature. Thermodynamic temperature differences are given by $\Delta T = \Delta T_A[(e^x - 1)^2/x^2 e^x]$, where $x = h\nu/kT_0$, h is the Planck constant, ν is the frequency, k is the Boltzmann constant, and $T_0 = 2.725$ K is the CMB temperature (Mather et al. 1999). A band-by-band tabulation of the conversion factor is given in Table 1.

Many sky regions are so strongly contaminated by foregrounds that a clean separation of the CMB is impossible, so in §2 we define a pixel mask to be used for CMB analyses. Microwave and other measurements show that, at high Galactic latitudes ($|b| > 15°$), CMB anisotropy dominates the Galactic signals in the frequency range $\sim 30 - 150$ GHz (Tegmark et al. 2000; Tegmark & Efstathiou 1996). This fact makes the use of the masks discussed in §2 attractive.

In §3 we address physical emission mechanisms that contribute to Galactic emission: synchrotron, free-free, thermal dust, and nonthermal (spinning or thermally fluctuating magnetic) dust emission. In §4 we demonstrate a method that combines the *WMAP* maps in such a way as to isolate the CMB. In §5 we separate the signals by emission type to better understand the foregrounds. Through a better understanding of the foregrounds we are able to demonstrate the degree of residual contamination for CMB analyses after masks are applied. We also improve our

understanding of the astrophysics of the foreground emission.

2. FOREGROUND MASKS

The purpose of a foreground mask is to exclude map pixels that contain "too much" foreground signal from use in CMB analyses. Some pixels often need to be masked even after a foreground reduction technique has been applied to a map. What constitutes "too much" foreground signal depends on the particular analysis. It is therefore useful to have masks available with different flux cut-off levels. For example, these masks can be used to demonstrate (in)sensitivity of scientific results to the level of foreground sky cut.

The mask cut-off level is always a compromise between eliminating foregrounds and preserving maximal usable sky area in analyses. The majority of excluded sky area in any mask is the Galactic plane region. The mask has the same pixel format as the map, where each mask pixel indicates whether or not the corresponding map pixel is to be used in analyses.

A successful mask should exclude those broad sky areas that are dominated by foregrounds, while leaving unexpunged the sky areas dominated by the CMB. Further, a useful recipe should be based on an unbiased process. *WMAP* has adopted a small set of standard masks of varying severity but with a common recipe. All masks are based on the K-band map since the foreground contamination is most severe in this lowest frequency band. The histogram distribution of all the pixel brightnesses in this map is strongly asymmetric in favor of positive pixel values because of the foreground contamination, as seen in Figure 1.

We reflect the (relatively uncontaminated) left side of the observed histogram about the mode. This symmetrized distribution is subtracted from the observed distribution, leaving a remainder, which is interpreted as contamination. The remainder histogram defines cutoff brightnesses.

The cutoff is applied to a low-resolution version of the K-band map in order to avoid excluding an archipelago of isolated pixels. *WMAP* images are generally pixelized with a HEALPix[1] N_{side} parameter of 512, whereas the masks are generated at $N_{side} = 64$. However, this procedure gives the mask a peculiar boundary inherited from the diamond-

[1]see http://www.eso.org/science/healpix/

Table 1. Conversion Factors and Selected Values by *WMAP* Band

	K-Band[a]	Ka-Band[a]	Q-Band[a]	V-Band[a]	W-Band[a]
Wavelength (mm)[a]	13	9.1	7.3	4.9	3.2
Frequency (GHz)[a]	23	33	41	61	94
$\Delta T/\Delta T_A$	1.014	1.029	1.044	1.100	1.251
T_A/I(R) (μK R^{-1})	11.4	5.23	3.28	1.40	0.56
T_A/EM (μK per cm^{-6} pc)	4.95	2.29	1.44	0.614	0.242

[a]Typical values for a radiometer are given. See text, Page et al. (2003b), and Jarosik et al. (2003) for exact values, which vary by radiometer.

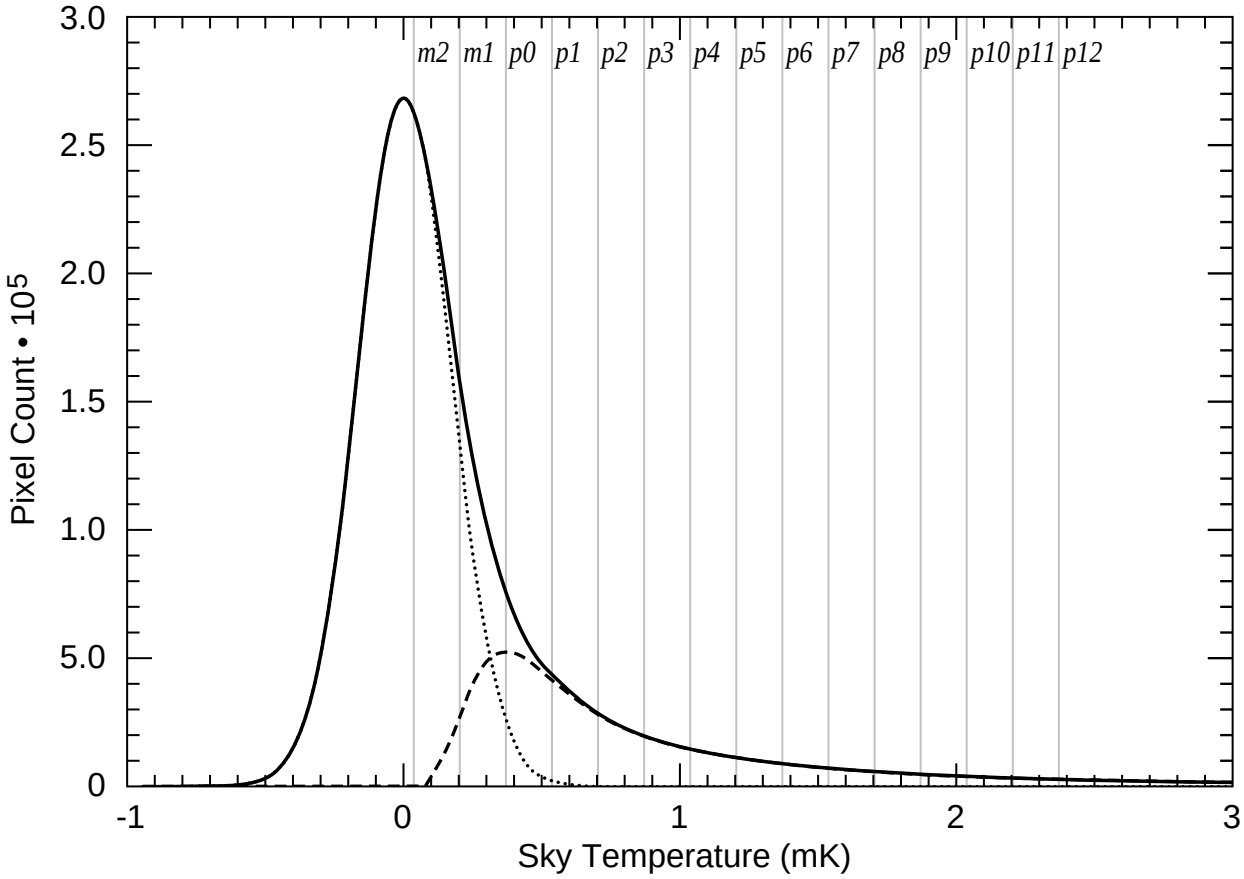

Fig. 1.— The solid curve is a histogram of pixel values in the K-band map. The dotted line is the symmetric reversal of the negative sky temperature portion of the solid curve about the peak value. The dashed curve is their difference or remainder, which is attributed to excess foreground emission. The peak of the remainder curve defines the K-band sky temperature cut-off for the mask that we call "Kp0". A series of masks with varying degrees of severity are likewise defined with "m" for "minus" and "p" for "plus", as shown. Temperature steps are defined by the rms half-width of the remainder histogram for values less than the mode.

shaped pixels. Accordingly, the boundary is softened by filtering the mask, which consists of ones and zeros, with a Gaussian of 2° full-width at half-maximum (FWHM), and taking the 0.5 contour of the result as the new mask boundary.

As explained above, a range of cutoff levels is desirable. A convenient step size in cut-off temperature is derived from the remainder histogram, shown in Figure 1, by using the root-mean-square (rms) half-width of this histogram for values less than the mode. A series of masks are made using multiples of these step sizes. A cut at the peak value of the remainder histogram is referred to as "p0". The sky cut used in any analysis is described by a symbolic name. For example, the mask defined by the peak of the remainder histogram using the K-band map is "Kp0". A mask with a temperature cut-off two steps smaller in temperature (more severe) is called "Km2", where "m" means "minus" and (for a less severe cut) "p" means "plus". Figure 2 shows selected masks based on the definitions in Figure 1. A separate set of masks based on bands other than K-band is not necessary since they correspond closely with specific K-band defined masks.

In addition to diffuse Galactic emission, point sources also contaminate the *WMAP* maps. We have constructed a point source source mask that includes: (1) all of the sources from Stickel et al. (1994) (which is the updated Kühr et al. (1981) 5 GHz 1 Jy compilation with attached optical source identifications); (2) sources with 22 GHz fluxes $\geq$ 0.5 Jy from the Hirabayashi et al. (2000) comprehensive compilation of flat spectrum AGN; (3) Additional flat spectrum objects from Teräsranta et al. (2001); and (4) sources from the X-ray/radio blazar survey of Perlman et al. (1998) and Landt et al. (2001). The mask excludes a radius of 0.6° about each of almost 700 source positions. Table 2 gives the percentages of the sky that are cut by each of the analysis masks with and without masking point sources.

Table 2. Percent Area Masked by Sky Cut Level.

Specification	% of pixels cut	% of pixels cut including point sources
Kp0	21.4	23.2
Kp2	13.1	15.0
Kp4	9.3	11.2
Kp12	3.8	5.8

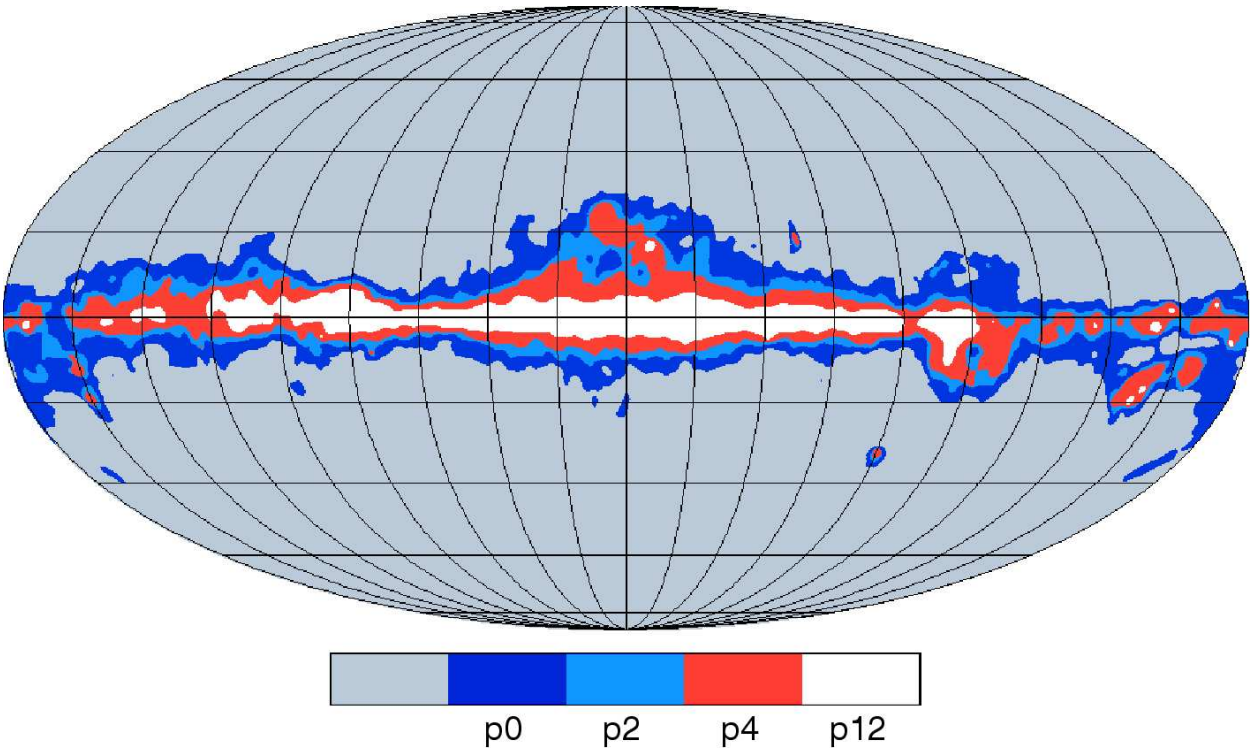

Fig. 2.— A full sky map of selected *WMAP* standard masks. The masking is based on the K-band signal levels, as discussed in §2. The series of masks allows for a choice of cut severity. (Each successive mask includes the previous regions; e.g., the p4 mask includes all of the pixels in the p12 mask.)

3. GALACTIC MICROWAVE EMISSION

We have two objectives. One is to fit and remove the foregrounds to derive CMB maps with well-specified levels of contamination. The second is to advance our understanding of the astrophysics of the foreground emission. In support of these two objectives, this section summarizes the astrophysical microwave emission mechanisms and relevant existing measurements.

3.1. Free-free emission

Free-free emission arises from electron-ion scattering. Free-free thermal emission has a $T_A \sim \nu^\beta$ high-frequency ($\nu > 10$ GHz) spectrum, with $\beta = -2.15$, and a low-frequency rise of $T_A \sim \nu^2$ due to optically thick self-absorption.

Radio astronomy provides no free-free emission map of the sky because free-free doesn't dominate the sky at any radio frequency. High-resolution, large-scale, maps of Hα (hydrogen n=3→2) emission (Dennison et al. 1998; Haffner et al. 2002; Reynolds et al. 2002; Gaustad et al. 2001) can serve as an approximate template for the free-free emission, except in regions of high interstellar dust optical depth, $\tau > 1$, at the Hα wavelength (about 16% of the sky). For $\tau \leq 1$, the Hα maps can be approximately corrected for the effects of extinction.

For T_e<550,000 K, the free-free volume emissivity is given by

$$\epsilon_\omega d\omega = \frac{8 n_e n_i Z^2 e^6}{3\pi\sqrt{2\pi} m^2 c^3} \sqrt{\frac{m}{kT_e}} \ln\left[\left(\frac{2kT_e}{\psi m}\right)^{3/2} \frac{2m}{\psi Z e^2 \omega}\right] d\omega \tag{1}$$

(Oster 1961), where T_e is the electron temperature, Ze is the net charge of the ion, $\psi = 1.78$ is from Euler's constant, m and e are the mass and charge of the electron, ω is the angular frequency of emission, and n_e and n_i are the electron and ion volume densities. We take $n_e = n_i$ and, for $T_e \approx 8000$ K (see, e.g., Otte et al. (2002)), it is safe to approximate $Z = 1$. We then use the definition of the emission measure, $EM = \int n_e^2 dl$, to get an expression for the *WMAP* free-free antenna temperature,

$$T_A^{WMAP}(\mu\mathrm{K}) = 1.44 EM_{\mathrm{cm^{-6}pc}} \times \frac{[1 + 0.22\ \ln(T_e/8000\ \mathrm{K}) - 0.14\ \ln(\nu/41\ \mathrm{GHz})]}{(\nu/41\ \mathrm{GHz})^2 (T_e/8000\ \mathrm{K})^{1/2}}. \tag{2}$$

Values of T_A/EM for the 5 *WMAP* bands are given in Table 1, assuming $T_e = 8000$ K.

The free-free spectral index for *WMAP* frequencies,

$$\beta_{ff}^{WMAP} = -2 - \frac{1}{10.48 + 1.5\ \ln(T_e/8000\mathrm{K}) - \ln \nu_{\mathrm{GHz}}} \tag{3}$$

does not extend to arbitrarily low frequency. In general, $T_A = T_e\ (1 - e^{-\tau_\nu})$. At the *WMAP* frequencies $T_A << T_e$, i.e. $\tau_\nu^{WMAP} << 1$, so $T_A^{WMAP} \approx \tau_\nu T_e$. Through this last relationship, we can use the *WMAP* measurement of T_A^{WMAP} to infer τ_ν and thus extend a predicted antenna temperature to low frequencies where $\tau_\nu \geq 1$. This can be done, for example, when comparing the *WMAP* free-free measurements in the Galactic plane to the Haslam et al. (1981) 408 MHz observations. The procedure is only approximate, however, since T_e and the beam filling factors for discrete sources are not accurately known.

The intensity of Hα emission is given by

$$I(\mathrm{R}) = 0.44\,\xi\,EM_{\mathrm{cm^{-6}pc}}\,(T_e/8000\mathrm{K})^{-0.5}\left[1-0.34\,\ln(T_e/8000\mathrm{K})\right], \tag{4}$$

where the Hα intensity is in units of Rayleighs (1 R = 2.42×10^{-7} ergs cm^{-2}s^{-1} sr^{-1} at the Hα wavelength of 0.6563 μm), the helium contribution is assumed to be small, and ξ is an extinction-correction factor. If, for example, the emitting gas is co-extensive with dust, then $\xi = \tau/[1-\exp(\tau)]$. H$\alpha$ is in R-band where the extinction is 0.75 times visible, $A_R/A_V = 0.75$. Thus, $A_R = 2.35E_{B-V}$, so $\tau = 2.2E_{B-V}$.

Finkbeiner (2003) assembled a full sky Hα map using data from several surveys: the Wisconsin H-Alpha Mapper (WHAM), the Virginia Tech Spectral-Line Survey (VTSS), and the Southern H-Alpha Sky Survey Atlas (SHASSA). This map, with the Schlegel et al. (1998) (hereafter referred to as SFD) extinction map of the sky, are used together to compute a best guess map of free-free emission in regions where $\tau<1$, under the assumption of co-extensive dust and ionized gas. The resulting template is shown in Figure 3(a).

We note that this template only approximates the free-free emission. There are several sources of uncertainty and error. For example: (a) Hα light scatters from dust grains in a manner unlike free-free; (b) There is uncertainty in the calibration of the Hα measurements, both within and between the observational groups; (c) There is some error in separating the geocoronal emission from the Hα line emission; (d) Any inaccuracy in the assumed Balmer atomic rates will also introduce error; (e) The Hα intensity depends on T_e, and it is not known precisely how T_e changes across the Galaxy; (f) There is uncertainty in ionization state of helium; (g) Any gas that has a sufficient bulk velocity could emit outside the bandwidth of the Hα observations; and (h) The extinction correction assumes that the Hα emission is co-extensive with the dust along the line of sight.

It would be difficult to assess and propagate all of the above sources of error. A comparison with a *WMAP* free-free map will be discussed in §5.

3.2. Synchrotron Emission

Synchrotron emission arises from the acceleration of cosmic ray electrons in magnetic fields. The acceleration occurs in Type Ib and Type II supernova remnants. The same $M>8\mathrm{M}_\odot$ stars that form these remnants also emit UV radiation that heats dust grains and ionizes hydrogen in the interstellar medium. Thus synchrotron emission is associated with the star-formation cycle.

The energy spectrum of cosmic ray electrons is expressed as a relativistic electron number density distribution $N(E)\sim E^{-\gamma}$. Since $N(E)$ varies across the galaxy, as does the magnetic field, **B**, the resulting synchrotron emission can be characterized by a wide range of spectral behaviors, and hence *the observed morphology of synchrotron sky maps will change substantially with frequency*. The synchrotron flux density spectral index, α, is related to the electron power law index, γ, by $\alpha = -(\gamma-1)/2$ at frequencies greater than a few GHz, where self-absorption is negligible.

The synchrotron emission spectrum is further affected by cosmic ray propagation, energy loss, and degree of confinement. Cosmic ray electrons can propagate via diffusion and/or convection. Diffusion involves the random scattering of cosmic ray electrons from varying magnetic fields, while convection implies the systematic outward movement of the sources of scattering.

Cosmic rays lose energy via synchrotron loss, inverse Compton scattering, adiabatic loss, and free-free loss. Cosmic ray electrons may be largely confined to their host galaxies, or may freely leave their halos. Highly confined cosmic ray electrons lose their energy before they escape from the halo of the galaxy, while poorly confined electrons escape the galaxy before they lose a substantial portion of their energy. A steep spectral index (e.g., $\alpha<-0.9$, $\beta<-2.9$)

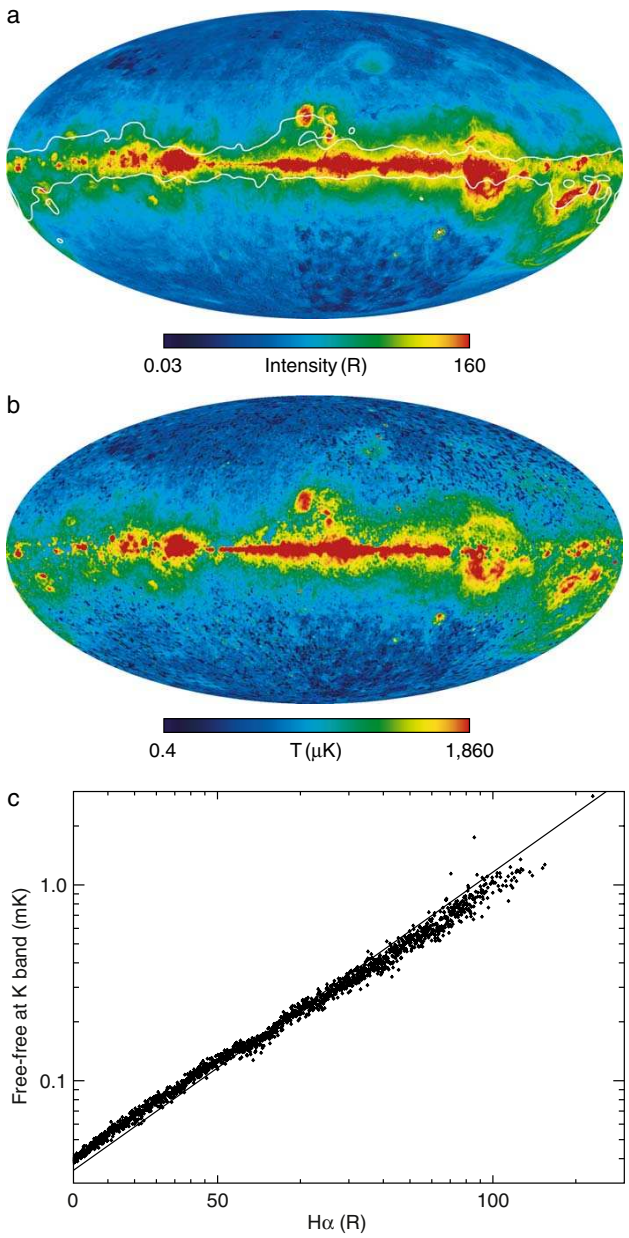

Fig. 3.— (a) A Hα map of the sky, corrected for extinction. The correction is only an approximation and is especially unreliable for regions where $\tau > 1$. These high opacity regions are roughly demarcated by the contour lines, which have been smoothed for clarity. (b) A full sky map of free-free emission based on the five bands of *WMAP* measurements. The map is the result of the MEM modeling process, as described in the text. (c) Pixel values in the MEM-derived free-free map are compared against their values in the Hα map, with each point representing an average in Hα intensity bins of ΔI = 8 R. The lack of scatter in the fainter bins reflects fidelity to the prior assumption of 11.4 μK/R at K-band. The data plotted only includes pixels where the Hα optical depth is estimated to be < 0.5 and the K-band antenna temperature is > 0.2 mK. The data are consistent with the μK/R values given in Table 1 within $\sim \pm 12\%$ uncertainty, depending on the fitting method used.

indicates a high rate of energy loss and a low escape rate. A flatter spectral index (e.g., $\alpha > -0.7$, $\beta > -2.7$) indicates that electrons can escape their host galaxy before losing a significant fraction of their energy. This can imply strong convection.

Synchrotron emission can be categorized as arising from two types of sources: electrons trapped in the magnetic fields of discrete supernova remnants and diffuse emission from cosmic ray electrons spread throughout the Galaxy. In a discrete supernova the magnetic field (typically $\sim 75\ \mu$G) is enhanced because it is frozen into the shocked compressed gas. The diffuse magnetic field in the Galaxy is typically only $1-5\ \mu$G.

Discrete supernova remnants typically have a spectral index of $\alpha \sim -0.5$ (i.e. $\gamma \sim 2$) in the few GHz radio range (Green 1988) (see also http://www.mrao.cam.ac.uk/surveys/snrs/snrs.info.html) and contribute only $\sim 10\%$ of the total synchrotron emission of the Galaxy at 1.5 GHz (Lisenfeld & Völk 2000; Biermann 1976; Ulvestad 1982), despite the enhanced magnetic field strength. More than 90% of the observed synchrotron emission arises from a diffuse component with a direction-dependent spectral index that generally lies in the range $-0.5 > \alpha > -1.1$ ($-2.5 > \beta > -3.1$ and $2.0 < \gamma < 3.2$). The cosmic ray electrons in the Galaxy substantially outlive their original supernova remnants and slowly lose energy while traveling large distances across the Galaxy.

The nonthermal spectral index is seen to steepen off the disk in our Galaxy and the same effect is seen in external galaxies. The observed steepening implies that energy loss is important (Lisenfeld & Völk 2000).

The low-frequency cut-off of synchrotron emission arises both from the single-electron synchrotron spectrum ($F(x) = x\int_x^\infty K_{5/3}(\xi)d\xi$, where $K_{5/3}$ is the modified Bessel function) low-frequency cut-off, and from self-absorption and free-free absorption, both of which become increasingly efficient at lower frequencies. The rise in the low-frequency synchrotron spectrum in the optically thick regime goes as $T_A \sim \nu^{2.5}$. Synchrotron emission is also cut-off by the Razin-Tsytovich effect, which describes a strong suppression of the synchrotron radiation when the phase velocity of the light in the plasma is greater than c. The synchrotron cut-off occurs at frequencies below where the kinetic temperature is equal to the brightness temperature. This often occurs at a frequencies of a few MHz, but can also play a role in GHz-peaked sources.

Synchrotron emission can be highly polarized, with the degree of linear polarization as high as $(3\gamma+3)/(3\gamma+7)$, i.e. $\sim 75\%$ polarized. This is almost never observed, however, due to Faraday rotation ($\propto \lambda^2$) and non-uniform magnetic field directions along a line of sight, which generally reduce the degree of observed polarization to $<20\%$.

Figure 4(a) shows the radio emission mapped over the full sky with moderate sensitivity at 408 MHz by Haslam et al. (1981). This map is dominated by synchrotron emission. Low frequency ($<$ 10 GHz) spectral studies of the synchrotron emission indicate that $\beta \approx -2.7$, although substantial variations from this mean occur across the sky (Reich & Reich 1988; Lawson et al. 1987). Higher energy cosmic ray electrons lose their energy faster than lower energy electrons, so the synchrotron spectral index steepens with time. Sometimes a "break" is seen in synchrotron spectra, which is useful for determining the age of the source. At frequencies above the break the spectral index steepens to $\alpha = -(2\gamma+1)/3$ due to synchrotron losses. This corresponds to an antenna temperature steepening of $\Delta\beta = -0.5$. Voelk (1989) predicts a break in the synchrotron spectrum of the Milky Way at 22 GHz, arising from a break in the relativistic electron spectrum at 20 GeV. Synchrotron steepening breaks with $\Delta\beta > -0.5$ have been observed in a few discrete sources (Green & Scheuer 1992; Morsi & Reich 1987), indicating additional processes beyond synchrotron losses.

Physical steepening effects compete against an observational measurement bias towards flat spectrum components. Steep spectral index synchrotron components seen at low radio frequencies become weak relative to flat spectral index components when observed at higher microwave frequencies. Thus it should be expected that flatter spectrum components will increasingly dominate in observations at higher microwave frequencies, even as all components may

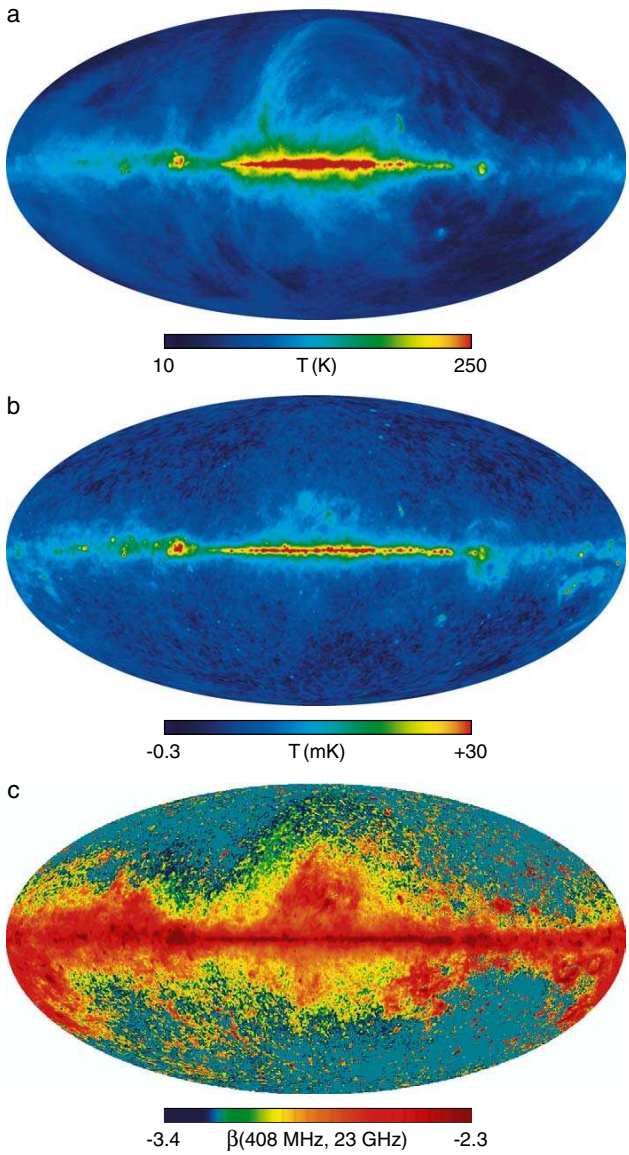

Fig. 4.— (a) The Haslam 408 MHz sky map is largely dominated by synchrotron emission. (b) The 23 GHz K-band *WMAP* map, also dominated by synchrotron emission, is more concentrated towards the plane than the 408 MHz Haslam map because flatter spectral index regions increasingly dominate at the higher observing frequencies. The steep spectral index North Galactic Spur, for example, is much less apparent at *WMAP* frequencies. The variable synchrotron spectral index across the sky renders the Haslam 408 MHz map an inaccurate tracer of synchrotron emission at microwave frequencies. (c) The spectral index map of $\beta(408\ \mathrm{MHz}, 23\ \mathrm{GHz})$ shows the flatter spectral index ($\beta \sim -2.5$) regions of active star-formation in the plane, where the cosmic ray electrons are generated. The steeper spectral index regions ($\beta \sim -3$) off the plane suggest the energy losses suffered by the cosmic ray electrons during the period of time required for their diffusion away from the star-formation regions of their origin. This spectral index map is dominated by synchrotron emission, but still contains free-free emission. It has been generated after setting zero-points based on cosecant fits to both maps, which provides an absolute zero-point for the *WMAP* map.

steepen.

The study of external galaxies can inform our picture of the Milky Way. For example, Hummel et al. (1991) present maps of the 610 MHz and 1.49 GHz emission from the edge-on spiral galaxy NGC891. They find that the synchrotron spectral index varies from $\beta \approx -2.6$ in most of the galactic plane to $\beta \approx -3.1$ in the halo. Thus, it is reasonable to expect similar spectral index variations in the Milky Way at ≈ 1 GHz. As one maps any such galaxy at increasingly higher frequencies the overall appearance will change considerably, with the flatter $\beta \approx -2.6$ plane emission increasingly dominating over the steeper spectral index halo.

In summary, *the synchrotron signal is complex. A large range of spectral indices are both expected and observed. Thus, any synchrotron template map of the sky will be frequency-dependent*. For many years CMB researchers have evaluated the synchrotron contamination level of their CMB data by examination of the Haslam-correlated amplitude scaled by $\beta \approx -2.75$. Given the expected and observed spectral index variability, this not necessarily sound.

3.3. Thermal Dust Emission and its Radio Correlation

Thermal dust emission has been mapped over the full sky in several infrared bands, most notably by the *COBE* and *IRAS* missions. A full sky template is provided by Schlegel et al. (1998) (SFD), and is extrapolated in frequency by Finkbeiner et al. (1999), hereafter referred to as FDS. This is shown in Figure 5(a).

Measurements of the thermal dust spectral index generally lie in the range $1.5 \leq \beta_d \leq 2$. For *WMAP* wavelengths, the FDS extrapolation predicts $\beta_d \approx 1.6$. Schwartz (1982) showed that there is an inverse relationship between the dust temperature and its spectral index. More recently, Dupac et al. (2001, 2002) have observed this inverse relation, in detail, in sources observed with the PRONAOS (PROgramme NAtional d'Observations Submillimetriques) 2-m balloon telescope at effective wavelengths of 200, 260, 360 and 580 μm. For dust temperatures below 20 K, Dupac et al. (2002) observe values in the range $1.6 \leq \beta_d \leq 2.5$ in M17. These steep values have implications for the grain material. They suggest emission from silicate grains such as $MgO{\cdot}SiO_2$ with $\beta_d \approx 2.5$ at ≈ 10 K (Agladze et al. 1996) or natural olivines such as fayalite ($Mg_xFe_{1-x}SiO_4$ with $x = 0.06$) (Mennella et al. 1998).

A remarkably tight correlation exists between the far-infrared and synchrotron emission of galaxies. This relation has been extensively studied and modeled (Dickey & Salpeter 1984; de Jong et al. 1985; Helou et al. 1985; Sanders & Mirabel 1985; Gavazzi et al. 1986; Hummel 1986; Wunderlich et al. 1987; Wunderlich & Klein 1988; Beck & Golla 1988; Fitt et al. 1988; Hummel et al. 1988; Mirabel & Sanders 1988; Bicay et al. 1989; Devereux & Eales 1989; Unger et al. 1989; Voelk 1989; Chi & Wolfendale 1990; Wunderlich & Klein 1991; Condon 1992; Bressan et al. 2002).

Bicay et al. (1989) comment that the synchrotron emission appears spatially smeared relative to the far-infrared distribution in galaxies. They suggest that this likely arises from the diffusion and/or convection of the cosmic ray electrons from their original site of star formation activity. If this is true, then one would expect higher frequency radio observations to become increasingly tightly correlated with the far-infrared distribution since the higher microwave frequencies preferentially sample the flatter spectrum, younger component.

Commenting on the synchrotron-dust correlation, Voelk (1989) predicts that, "...whether integral or local, the correlation should also become better for smaller wavelengths of observation. The reason is that a decreasing wavelength implies higher energies of the radiating electrons. These electrons lose energy faster and therefore are more localized around their sources."

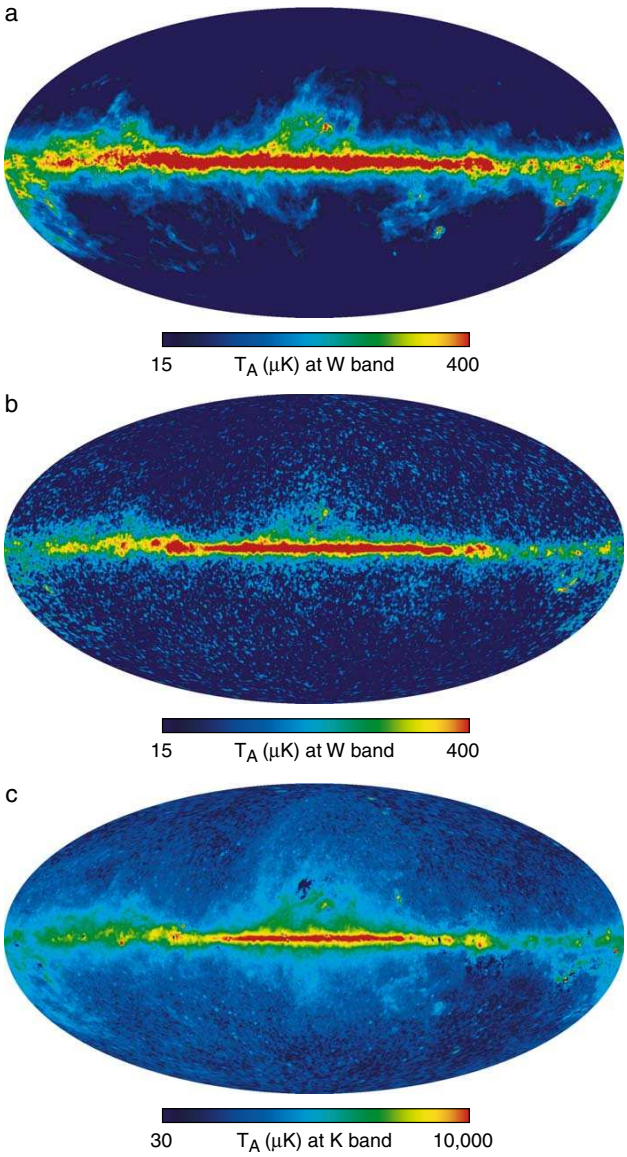

Fig. 5.— (a) The FDS dust map at 94 GHz based on data from *IRAS* and *COBE*. This map is used as a prior in the MEM fit. (b) The full sky thermal dust map from the MEM procedure run on the five band *WMAP* data and shown for W-band. The morphology is found to be similar both to the expectation (prior), in (a) and to the synchrotron result map, in (c). (c) This full sky map of synchrotron emission referred to K-band is based on the five bands of *WMAP* measurements. The map is the result of the MEM modeling process, as described in the text. Note the rough similarity of the microwave synchrotron emission to the thermal dust emission. This is presumed to be a result of their common origin in regions of star-formation.

3.4. Spinning and Magnetic Dust Emission

In addition to the thermal emission from dust, above, there are various other ways in which dust can radiate at microwave wavelengths. These include electric dipole emission from spinning dust grains and magnetic dipole emission from thermally fluctuating dust grains (Erickson 1957; Draine & Lazarian 1999, 1998a,b). Emission from spinning dust can produce $\beta \sim -2$ from 20-40 GHz. The high-frequency cut-off of spinning dust emission is due to the limited speed at which a dust grain can spin.

All theories to explain the amazingly tight correlation between radio and far-infrared emission from galaxy to galaxy relate to the level of the star formation activity. The star formation cycle forms and destroys dust grains, heats the grains, creates magnetic fields and relativistic electrons, and creates the O- and B-stars that ionize the gas. The tight correlation persists down to very low radio frequencies, yet the radio emission can not be due to spinning dust gains since they do not radiate strongly at such long wavelengths. This suggests that radio/microwave emission and thermal dust emission are tightly correlated, not because of a common dust emission source, but rather as a result of the fact that both trace star-formation activity. While spinning dust emission is not a dominant source of $\sim$ 1 GHz radio emission in the Galaxy, it may be significant at higher microwave frequencies ($\sim$ 30 GHz).

Finkbeiner et al. (2002) searched for spinning dust emission in ten discrete Galactic sources at 5, 8, and 10 GHz. No detection was reported for 8 of the 10 sources, implying that spinning dust emission is not a ubiquitous and dominant emission mechanism in our Galaxy. Two of the ten sources were reported "tentative" detections. They caution that a solid detection would require observations of the predicted spectral roll off both at high and low frequencies.

It is reasonable to assume that the Milky Way should be like other spiral galaxies and, in particular, the microwave properties of external galaxies should help elucidate the global properties of the Milky Way. Klein & Emerson (1981) report the spectra of 16 spiral galaxies to frequencies up to 10.7 GHz. They find that the spectral index, averaged over the 16 galaxies, is well described by a single synchrotron power law spectral index of $\beta = -2.71 \pm 0.08$. Gioia et al. (1982) report that the mean spectrum of 56 bright spiral galaxies is dominated by synchrotron emission, with a small additional free-free emission component. They report that a free-free plus single power-law synchrotron fit fully explains their observations. Niklas et al. (1997) examine 74 Shapley-Ames galaxies and they also find their spectra dominated by a power-law synchrotron index with some free-free emission. These extragalactic studies report no suggestion of anomalous sources of emission. The main impediment to stronger statements about spinning dust emission in external galaxies is the (perhaps surprising) sparsity of microwave observations of normal galaxies at microwave frequencies greater than $\sim$ 10 GHz.

4. INTERNAL LINEAR COMBINATION OF THE MULTIFREQUENCY *WMAP* MAPS

Linear combinations of the multi-frequency *WMAP* sky maps can be formed using constraints so that the response to Galactic signals is approximately canceled while maintaining unit response to the CMB. Linear combinations of multi-frequency data need not rely on assumptions about the foreground signal strengths of the various emission mechanisms. An advantage of this method is that it is "internal", that is, it relies only on *WMAP* data, so the calibration and systematic errors of other experiments do not enter.

We create a CMB map by computing a weighted combination of the maps that have been band-averaged within each of the five *WMAP* frequency bands, all smoothed to 1° resolution. Weights can be determined by minimizing the variance of the measured temperatures subject to the constraint that the weights add to one, thus preserving unit response to the thermal CMB spectrum.

When the entire sky is treated with a single set of weights, imperfections are apparent due to the fact that the foreground properties (i.e., spectral indices) have significant spatial variation, especially within the inner Galactic plane. Thus, to improve the result, the inner Galactic plane is divided into 11 separate regions, within which weights are determined independently. All but one of the $N = 12$ total regions are thus in the inner Galactic plane, within the Kp2 cut. The temperature (in CMB thermodynamic units) of each pixel, p, in each region $n = 1, 2, \ldots N$ is

$$T_n(p) = \sum_{i=1}^{5} \zeta_{n,i} T^i(p), \tag{5}$$

where the sum is over the five *WMAP* bands. The weights, ζ, for each region are determined by carrying out a nonlinear search for the minimum of var(T_n) within each of the N regions of the sky, subject to the constraint that

$$\sum_{i=1}^{5} \zeta_i = 1, \tag{6}$$

thus preserving only signals with a CMB spectrum. For the region that covers the full sky outside of the inner Galactic plane, the weights are $\zeta = 0.109, -0.684, -0.096, 1.921, -0.250$ for K, Ka, Q, V, and W bands, respectively.

This process creates a map with slight discontinuities at the region boundaries since each region, R_n, is treated independently. To smooth these discontinuities, we create a set of N maps, with weights $w_n(p) = 1$ for $p \in R_n$ and $w_n(p) = 0$ for all other p. We then smooth these $N = 12$ maps of $w_n(p)$ (containing only ones and zeros) using a $1\overset{\circ}{.}5$ smoothing kernel. The final map is then given by the weighted combination

$$T(p) = \sum_{n=1}^{N} w_n(p) T_n(p) \Big/ \sum_{n=1}^{N} w_n(p), \tag{7}$$

which greatly reduces boundary effects. The resulting CMB map is shown in Figure 6(a).

5. MAXIMUM ENTROPY METHOD (MEM) SPATIAL AND SPECTRAL FIT

In §4 the objective was to cancel the Galactic signal, regardless of its nature. In this section we attempt to distinguish and understand the different emission sources. It is a coincidence of nature that there are three known emission mechanisms that are each capable of generating similar spectra in the microwave spectral regime. Free-free, synchrotron, and spinning dust emission can all have a spectral index of $\beta \sim -2$ at the *WMAP* frequencies. The key to separating these is to use data from outside the microwave spectral regime.

Recent observations of Hα emission over large regions of the sky can help trace free-free emission. This is especially useful in regions where the extinction of Hα is small, largely at high Galactic latitudes. The 408 MHz radio map (Haslam et al. 1981) is at a sufficiently low frequency that spinning dust emission is negligible.

We formulate a model temperature solution at each frequency band and each pixel, p, as

$$T_m(\nu, p) = S_{cmb}(\nu|p) T_{cmb}(p) + S_s(\nu|p) T_s(p) + S_{ff}(\nu|p) T_{ff}(p) + S_d(\nu|p) T_d(p) \tag{8}$$

where cmb, s, ff, and d represent the CMB, synchrotron (plus spinning dust), free-free, and thermal dust components, respectively. $S_c(\nu|p)$ is the spectrum of emission c in pixel p, and is not necessarily uniform across the sky. $T_c(p)$ is the spatial distribution of emission type c, where synchrotron (plus spinning dust) and free-free are normalized

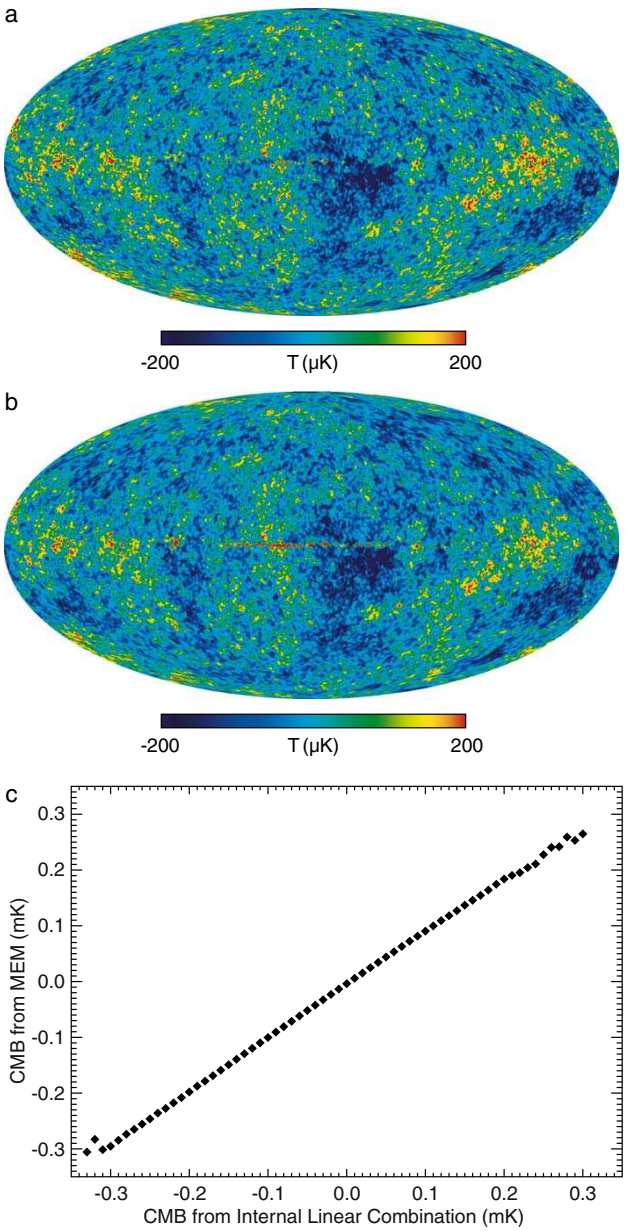

Fig. 6.— (a) A *WMAP* CMB full sky map derived from an internal combination of the *WMAP* data with no use of external data sets, as described in §4. (b) The full sky CMB map that results from the MEM procedure, as described in §5. (c) The plot is a binned pixel-by-pixel comparison of the MEM-derived CMB map with the CMB map derived by the minimum variance combination technique.

to the *WMAP* K-band temperature, and thermal dust is normalized at W-band. The model is fit by minimizing the functional $H(p) = A(p) + \lambda(p)B(p)$ (Press et al. 1992), where λ is a regularizing parameter, $A(p) = \chi^2(p) = \sum_\nu [T(\nu,p) - T_m(\nu,p)]^2/\sigma^2$ is a pixel by pixel fit, and $B(p) = \sum_c T_c(p) \ln[T_c(p)/P_c(p)]$ sums only over Galactic emission components. $P_c(p)$ is a prior model of the spatial distribution of the temperature of emission component, c, normalized to the same frequency as T_c. The MEM parameter λ controls the fidelity of the fit to the a priori model. The form of B ensures the positivity of the Galactic emission $T_c(p)$, which greatly alleviates degeneracy between the foreground components. The formalism is unaware, for example, of the different physics of synchrotron versus spinning dust emission.

We begin by smoothing all maps to a uniform 1° resolution. Initially we subtract the internal combination CMB map derived in §4 from the five *WMAP* maps to remove this part from the fit. Since *WMAP* measures only differentially on the sky it does not determine a meaningful zero level for the maps. For each of the 5 maps, we use the mean observed temperature variations with Galactic latitude to estimate the zero level, assuming a plane-parallel model for the Galactic emission. This is done by adding an offset to each map such that a fit of the form $T = A \csc b + B$ over the range $-90° < b < -15°$ yields a value of zero for the intercept, B. For consistency we treat the 408 MHz map the same way. Figure 7 shows fits of this form for $b < -15°$ and for $b > 15°$. The results for the Southern sky are chosen because they minimize the number of negative pixel values in the 408 MHz map.

The prior spatial distribution maps, $P_c(p)$, are chosen as follows. For synchrotron emission we use the Haslam map scaled to K-band using $\beta_s = -2.9$. For free-free, we use the full sky Hα map produced by Finkbeiner, scaled to K-band antenna temperature using 11.4 μK R^{-1}. The dust prior is taken to be "Model 8" of FDS, evaluated at 94 GHz. These priors are fixed, but we have evaluated the sensitivity of the output solution to the choice of prior and, as discussed below, have used the results to guide the choice of the regularizing parameter λ.

We construct initial spectral models, $S_c(\nu|p)$, as follows. From the 408 MHz map (Figure 4a) and the *WMAP* K-band map (Figure 4b) we construct the β(408 MHz, 23 GHz) spectral index map in Figure 4c. This is largely a synchrotron spectral index map, but with some free-free and spinning dust contribution. Significant variations are seen in this spectral index across the sky. The initial model for $S_s(\nu|p)$ is $(\nu/\nu_K)^{\beta(p)-0.2}$ where $\beta(p)$ is the above spectral index map. For the free-free and dust, we take the initial models to be $S_{ff}(\nu) = (\nu/\nu_K)^{-2.15}$ and $S_d(\nu) = (\nu/\nu_W)^{+2.2}$ respectively. The latter choice for the dust model was informed by many previous trial models.

In general, for a given set of spectral models, the MEM solution has residual errors. Since the synchrotron and dust spectra are poorly known at microwave frequencies, we use the model residuals to guide an update of the synchrotron and dust spectral models, S_s and S_d in an iterative fashion. Specifically, after each minimization of $H(p)$, we update S_s and S_d as follows

$$T_s S_s(\nu|p) \rightarrow T_s S_s(\nu|p) + g \cdot R(\nu,p) \qquad \text{K} - \text{V bands} \tag{9}$$

$$T_d S_d(\nu|p) \rightarrow T_d S_d(\nu|p) + g \cdot R(\nu,p) \qquad \text{W band} \tag{10}$$

where $R(\nu,p) = T(\nu,p) - T_m(\nu,p)$ is the solution residual (data minus model), and g is a gain factor ($g \leq 1$). Each spectral model is renormalized to 1 at its fiducial frequency prior to running a new minimization of $H(p)$. To stabilize the MEM computations at frequencies where individual components are weak, and thus poorly determined, we extend the synchrotron power law spectral index between Q-band and V-band to W-band. Likewise, we extend the dust index between W- and V-bands to Q-, Ka-, and K-bands. The extension is re-applied at every iterative step.

The regularizing parameter, λ, controls the degree to which the solution follows the prior. Note that $\lambda(p)$ can vary across the sky since the fits are performed independently for each pixel. Our philosophy is that the *WMAP* data should take priority over the priors in sky regions where the *WMAP* signal-to-noise ratio is high and that the priors should take priority where the *WMAP* signal-to-noise ratios are too low. After some trial-and-error, we arrive at a map of $\lambda(p)$ values that implement this, $\lambda(p) = 0.6\,(T/1\text{ mK})^{-1.5}$, where T is the K-band antenna temperature in mK.

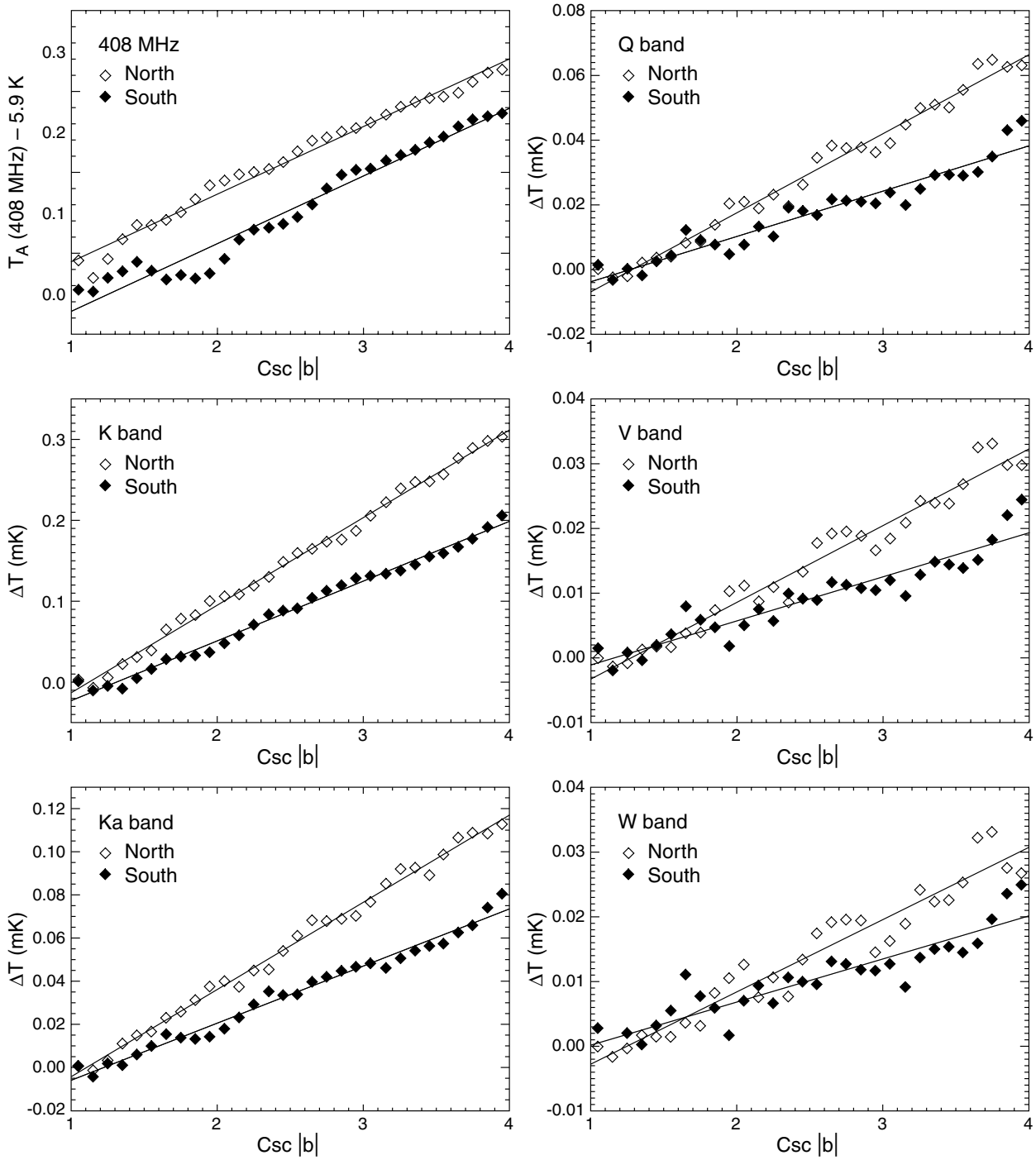

Fig. 7.— A plane-parallel cosecant model gives a fairly good fit to the 408 MHz Haslam map and the five frequency *WMAP* maps. Application of a cosecant fit is used to set the zero-points of the *WMAP* maps in a self-consistent manner. The Southern fit is used to minimize the number of negative map temperatures. Each panel shows linear fits to data averaged over bins in csc(b) for both Northern and Southern Galactic latitudes. For the Northern latitudes, the longitude range covering the North Polar Spur was excluded. A 5.9 K extragalactic correction (Lawson et al. 1987) was subtracted from the 408 MHz data, and the *WMAP* data shown here were normalized such that the mean intensity at the Galactic poles is zero.

This choice makes $\lambda(p)$ vary continuously between ~ 3 where the K-band signal is noisy and ~ 0.2 where the K-band signal is strong. The results are not strongly sensitive to the exact form of $\lambda(p)$. Similar results were obtained with $\lambda = 0.2$ everywhere, but the results are noisy where the *WMAP* signal is weak. Using $\lambda > 3$ everywhere produces results that are somewhat dependent on the priors, P, in regions of high signal-to-noise ratio.

We run the MEM code to minimize H. We typically iterate (residual errors fed back to improve the solutions) ~ 10 times with a feedback gain factor of $g = 0.5$ per iteration to produce overall residuals $< 1\%$. The results of the MEM are shown in Figures 3, 5, and 8. Note that minimal residuals and reasonable results are achieved without the introduction of any unmodeled Galactic component. Figure 5 shows that there is a fairly close spatial correlation between synchrotron and thermal dust emission at microwave wavelengths. Figure 9 is a histogram of the synchrotron and/or spinning dust component. The spectral index looks very much like synchrotron emission with a 0.5 steepening of the index from synchrotron losses, as predicted by Voelk (1989) based on the observed break in the relativistic electron spectrum in the solar neighborhood. A spinning dust component would flatten the index from β(408 MHz, K) to β(K , Ka). The fact that the fit index steepens means that any spinning dust emission component is subdominant. We limit the overall spinning dust emission to $< 5\%$ of the total antenna temperature at Ka-band based on the observed spectrum and the Draine & Lazarian (1998b) model. The thermal dust spectral index histogram, shown in Figure 9, indicates $\beta_d \approx 2.2 \pm 0.1$.

We freeze the spectral models S_s, S_{ff}, and S_d once small residuals are achieved, and the improvement in the residuals is not significant. We then introduce the CMB as a model component with a known spectral index, $S_{cmb}(\nu|p) = dB/dT$ for a Planck function B with $T_0 = 2.725$ K, and iterate again to solve for a CMB map and modified component amplitude maps. The MEM-derived CMB map is shown in Figure 6b and a binned pixel-by-pixel comparison with the internal combination CMB map is shown in Figure 6c. It is not surprising that the MEM CMB map agrees well with the linear combination map since the foreground components were derived based on low residuals with respect to the subtracted linear combination CMB map. Yet, by giving the component amplitudes an opportunity to re-adjust with the CMB amplitudes as a new degree of freedom, it is a reassuring cross-check that the solutions are generally unaffected. Small ($\approx 1\%$) errors seen in the Galactic plane of the MEM CMB map relative to the combination CMB map illustrate the residual uncertainty of the MEM solution.

Low residual solutions are highly constrained, but not necessarily unique or correct. Loosely speaking, the model must account for a considerable signal amplitude in K-band and very little total amplitude in V-band. This constrains the synchrotron spectral index to be steep. Likewise, the model must match the dust signal in W-band, but the dust spectral index must be steep enough to stay under the total signal level in V-band. The free-free level can be thought of as making up the remainder of the V-band signal after the synchrotron and dust have been fit. Any additional emission components are strongly disfavored due to the already low total V-band signal. Limitations in the precision and accuracy of the Hα measurements, uncertainty in the degree of Hα extinction, and the uncertainty in the conversion factor between Hα and free-free, combine so as to not allow the free-free to be fixed with sufficient precision to achieve a uniquely "correct" MEM solution. Figure 3c shows a (bin-averaged) pixel-by-pixel comparison of the MEM free-free result with the Hα prior. The slope is within $\pm 12\%$ (depending on the method of fit) of the expected value from §3.1 and Table 1, meaning that the model can not be far off what is physically reasonable.

The total observed Galactic emission matches the MEM model to $< 1\%$ while emission is separated into the individual components with a few percent accuracy. An overview of the Galactic spectra and spatial power is shown in Figure 10. The total flux of our Galaxy ($F_\nu = \int I_\nu(l,b) \cos l \cos b \, d\Omega$) in the five *WMAP* bands is 45, 38, 35, 32, and 48 kJy, from K-band to W-band. Thus, we present a "reasonable" model that conveys far more information about the microwave foregrounds than was previously known.

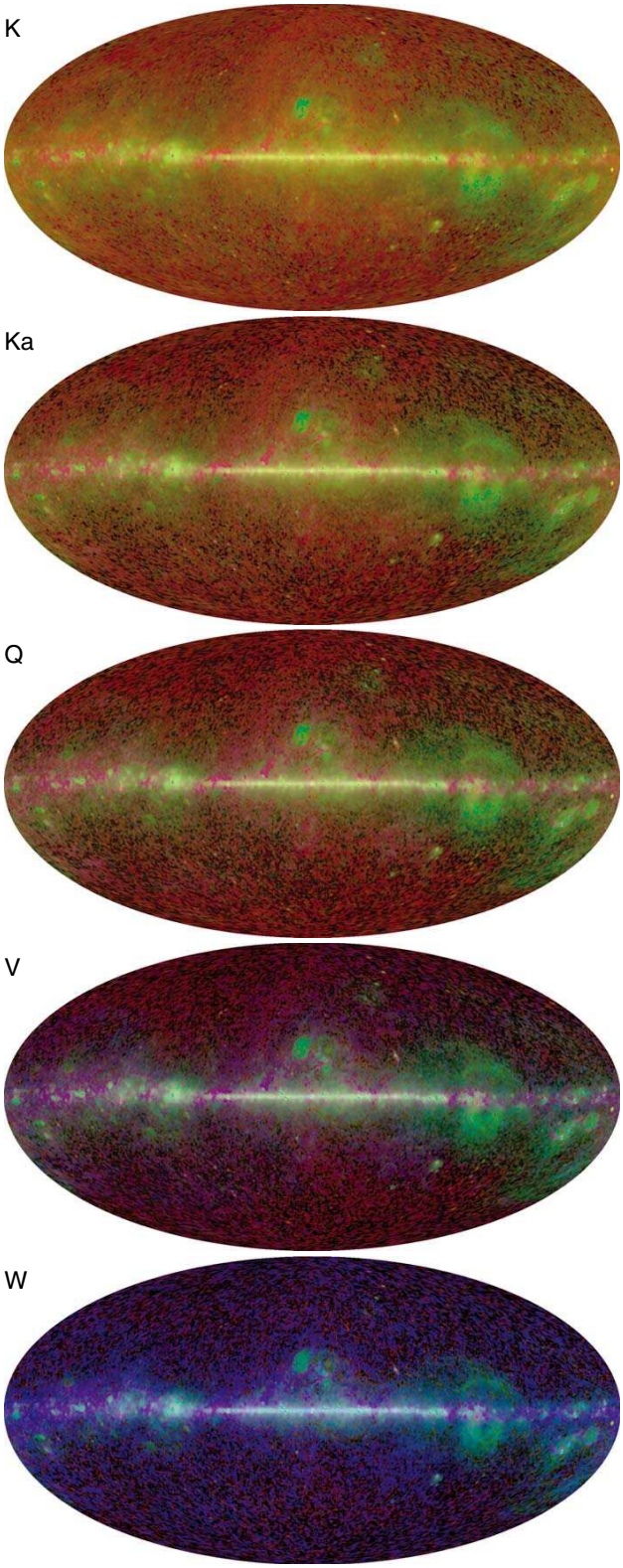

Fig. 8.— Three color maps of the Galactic emission from the the MEM model for K-band (top) through W-band (bottom). These maps give a feeling for which emission mechanism dominates as a function of frequency and sky position. Synchrotron is red, free-free is green, and the thermal dust is blue.

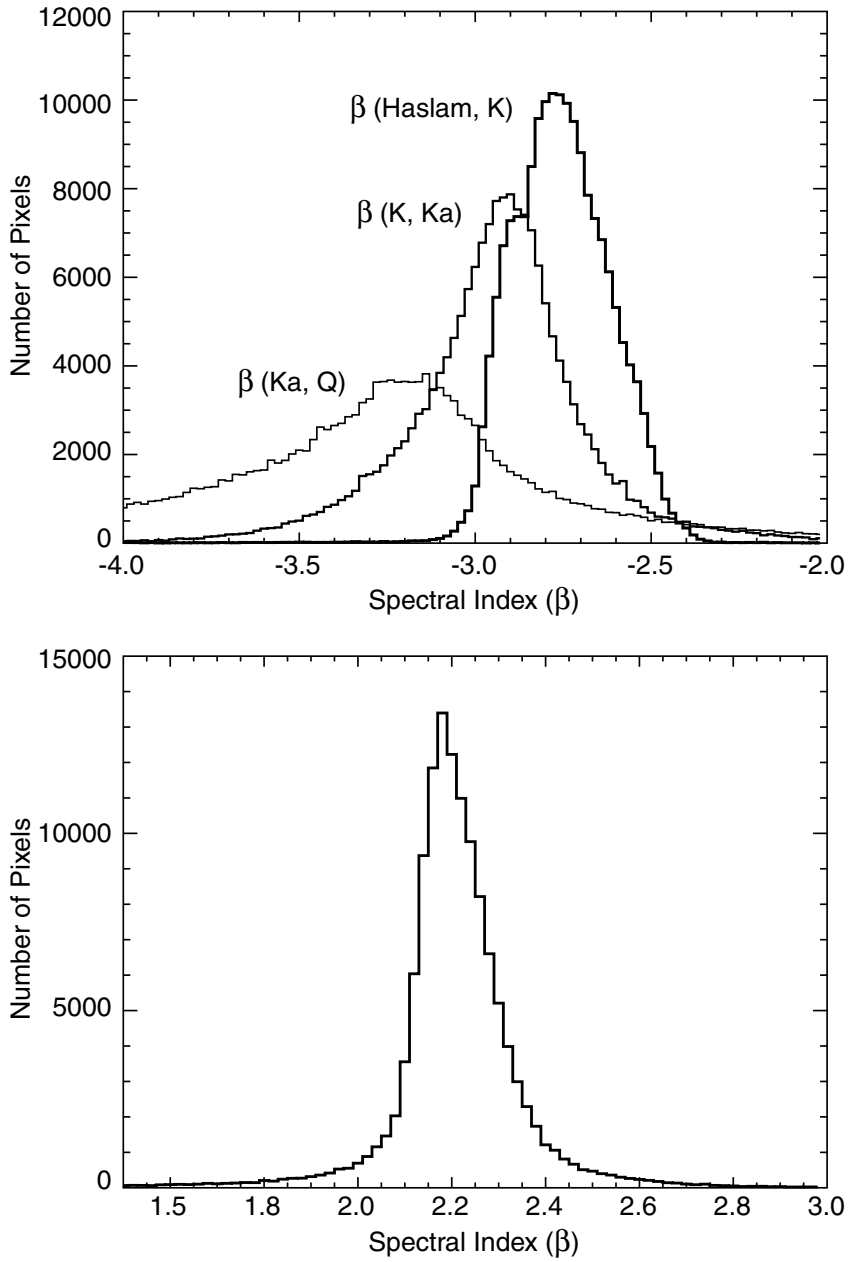

Fig. 9.— *Top*: Spectral index histograms of the MEM-fit low frequency component. Lower amplitudes and increased widths of distributions are indicative of lower signal-to-noise ratios rather than physical effects. The histogram only includes pixel values where the total K-band antenna temperature is T_A(K-band)$> 500\mu$K to minimize low signal-to-noise artifacts. The steep spectral index $\beta \sim -2.75$ between the Haslam 408 MHz measurements and the *WMAP* MEM solution at K-band is seen to steepen further in going from K-band to Ka-band and even further still to Q-band. The total steepening of $\Delta\beta \approx -0.5$ is highly suggestive of synchrotron emission with a synchrotron loss spectral break near K-band. There is no evidence for the spectral flattening expected from spinning dust emission. We can thus limit spinning dust emission to $< 5\%$ of the overall Ka-band signal. *Bottom*: Spectral index histogram of the MEM-fit dust component. The MEM fit to thermal emission from dust gives a spectral index of $\beta_d \approx 2.2 \pm 0.1$ between V-band and W-band. The wings of the distribution are dominated by signal-to-noise limitations.

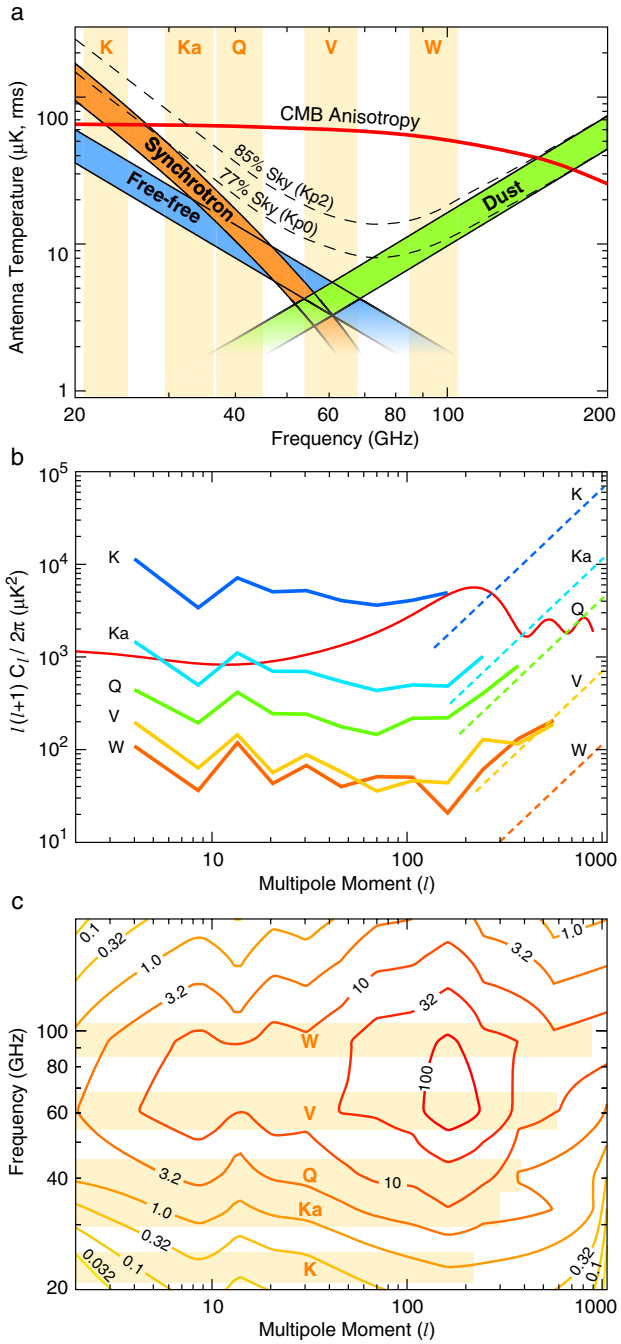

Fig. 10.— CMB versus Foreground Anisotropy. The *WMAP* frequency bands were chosen to be in a spectral region where the CMB anisotropy is most dominant over the competing Galactic and extragalactic foreground emission. This can now be quantified for *WMAP* and future experiments. (a) Spectra are shown of the CMB anisotropy and the Galactic emission from the MEM modeling. (b) The foreground power spectra are shown for each *WMAP* band using the Kp2 mask. The power spectra within frequency bands are derived as cross-power spectra between radiometers minus the *WMAP*-derived CMB model. In K- and Ka-band, where cross-power spectra are not available, the noise bias has been estimated and subtracted. The band-by-band point source fits to an l^2 term are shown in the dashed lines on the right. The power spectra are expected to asymptotically join these lines. Note that the total foreground power spectra (excluding point sources) go as $C_l \sim l^{-2}$. (c) The contour plot shows the ratio of CMB to foreground anisotropy power as a function of frequency and multipole moment for the Kp2 mask.

6. TEMPLATE FITS

While the MEM method, discussed above in §5, produces a CMB map, it is not straightforward to use that map for cosmological analyses since its noise properties are complicated. The MEM method is much more valuable for understanding the physical nature of the foregrounds than for producing a CMB map useful for CMB analysis.

To produce a CMB map useful for cosmological analyses (by maintaining well specified noise properties) we simultaneously fit (outside the Kp2 cut) a set of externally derived template maps to the *WMAP* maps. The template maps are the Hα map (corrected for an estimate of extinction), the 408 MHz Haslam map, and the FDS 94 GHz dust map. The resulting coefficients are given in Table 3. A constant term is included in the fits.

The rising amplitude of the dust template fit coefficient with decreasing frequency has been interpreted by some as evidence of spinning dust emission. We have learned from the MEM solutions in §5, however, that the 408 MHz Haslam map is not a high-fidelity synchrotron template at the *WMAP* frequencies due to the strongly variable spectral index across the sky. This is reflected in the negative template coefficients in V- and W-bands. From the point of view of removing foreground emission for CMB analyses, we are not concerned about the degeneracy that exists between the strongly correlated dust and synchrotron emission components. We are only concerned with reducing the foreground level.

To further investigate past results on dust-correlated radio emission we fit the FDS thermal dust template to the total MEM Galactic model (synchrotron plus free-free plus thermal dust emission) for each *WMAP* band, using the Kp2 cut. We then compute the spectral index of the dust-correlated emission. We use the *WMAP* Ka and V bands to approximate the *COBE* DMR 31 GHz and 53 GHz bands. The result is β(31 GHz, 53 GHz) $\approx \beta$(Ka, V)= –2.2. This replicates the previous dust-correlated radio emission. Physically, the –2.2 index is a combination of a $\beta \approx -3$ synchrotron component that is correlated with thermal dust (because of star-formation activity) combined with the $\beta = +2.2$ thermal dust component. This combined index gets much steeper at lower frequencies (where the dust emission is weak) and is much flatter at higher frequencies where the synchrotron and free-free become weak relative to thermal dust emission.

An alternative fitting method is used in the current first-year *WMAP* CMB analyses to avoid negative coefficients for the synchrotron component, above. Only the Q-, V-, and W-band data are included. The dust component is fitted separately to each band (3 parameters). A single amplitude is used to fit the free-free emission across all three bands, assuming a spectral index $\beta = -2.15$. Similarly, a single amplitude is used for the synchrotron emission, $\beta = -2.7$. Thus, five parameters are used: dust amplitudes in the Q-, V-, and W-bands (0.582, 0.974, and 0.528, respectively), a free-free amplitude (0.851), and a synchrotron amplitude (1.175). The units of the coefficients are the same as in Table 3, with the free-free and synchrotron amplitudes referred to Q-band.

Although this template method is not particularly physical, it does remove the Galactic foreground outside the Kp2 cut sufficiently for CMB analyses, as shown in Figure 11. We estimate the residual contamination in two ways. By examining deviations from a Gaussian distribution, we estimate that the template subtraction reduces the Galactic signal rms (after the sky cut) by 86% in Q-band, 81% in V-band, and 84% in W-band. This agrees well with a power spectrum estimate in the range $2 < l < 100$ before and after the template subtraction. We estimate that the Galactic contamination has gone from 32% of the CMB power to 2.2% of the power in Q-band, from 7.2% to 0.8% in V-band, and from 11% to $< 0.4\%$ in W-band. See Hinshaw et al. (2003) for the power spectra before and after the template subtraction.

This method was adopted before the MEM solutions were available to allow the CMB work to proceed in parallel with the Galaxy work and thus to enable a timely release of data products to the scientific community. Future analyses will likely use a modified approach, but *we caution that the MEM results cannot be applied directly to CMB analyses*

Table 3. Template Fits to the *WMAP* Maps: Coefficients and Percent Fit by External Template

Band	Dust:FDS (rel to FDS)	Free-Free:Hα (μK/R)	Synchrotron:Haslam (μK/K)	FDS[a] (%)	Hα[a] (%)	Haslam[a] (%)
K	6.3	4.6	5.6	60	14	26
Ka	2.4	2.1	1.5	64	18	18
Q1	1.5	1.3	0.5	69	20	11
Q2	1.4	1.3	0.5	68	20	12
V1	0.9	0.5	-0.2	92	15	–8
V2	0.9	0.4	-0.2	95	13	–8
W1	1.2	0.1	-0.3	113	3	–16
W2	1.2	0.1	-0.4	113	4	–17
W3	1.2	0.1	-0.3	112	2	–14
W4	1.1	0.1	-0.3	112	4	–16

[a]The percentages are estimates of how the total fit signal breaks down into the three templates, for each frequency band.

Table 4. *WMAP* Point Source Counts

Band	Flux Range (Jy)	$N_{\rm src}$	κ (Jy^{-1} sr^{-1})	β
K	2-10	72	45 ± 12	-2.8 ± 0.2
Ka	2-10	73	44 ± 12	-2.8 ± 0.2
Q	2-10	61	32 ± 9	-2.7 ± 0.2

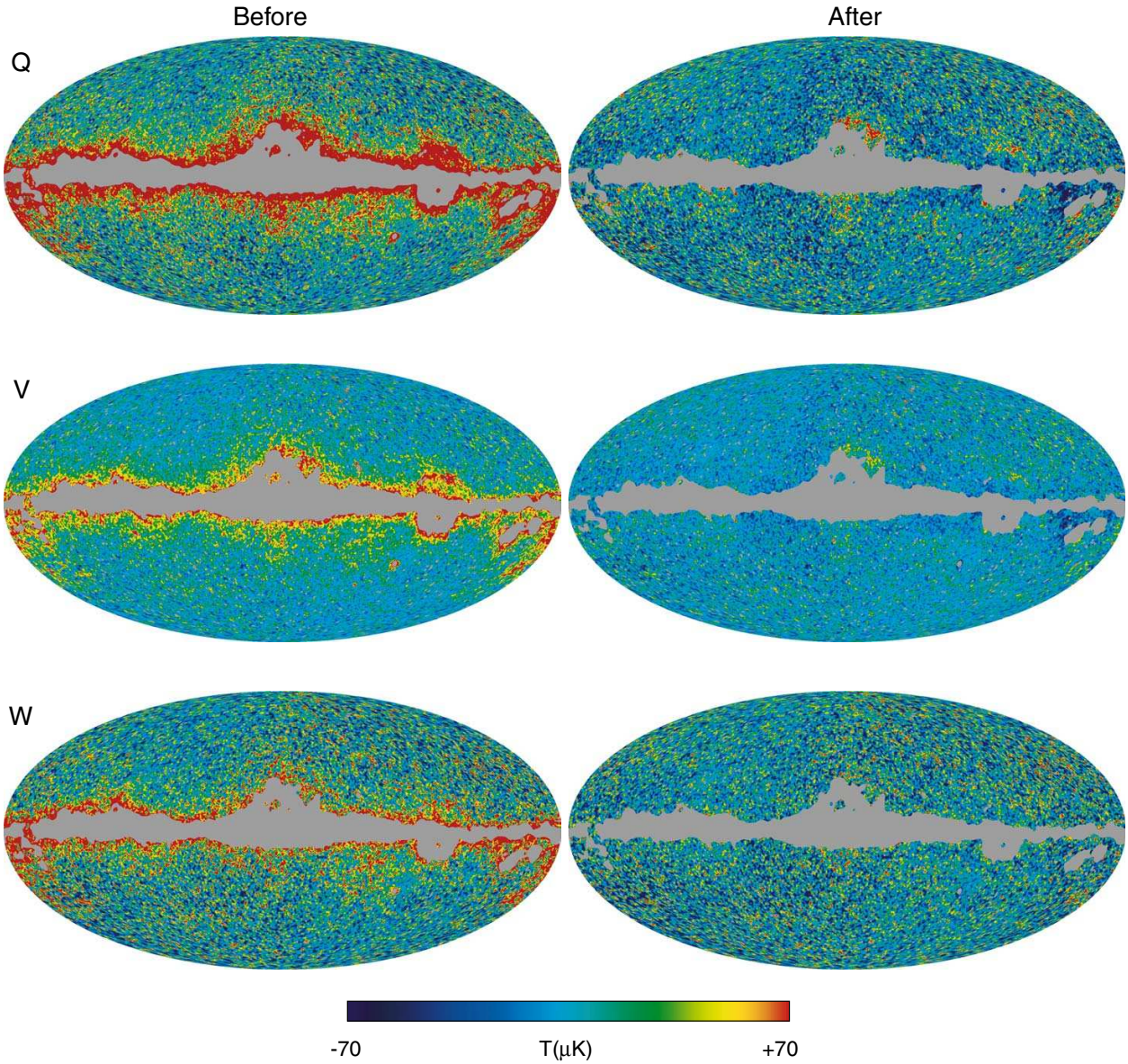

Fig. 11.— The Q-, V-, and W-band maps, in CMB thermodynamic temperature, are shown with the Kp2 mask applied and a CMB estimate, from Fig 6 (a), removed. These maps are individually fit to template maps of synchrotron, dust, and free-free emission to remove residual foreground contamination. Reduction of foreground emission after template fitting is also shown. The foreground reduction works well, despite the fact that the Haslam map is a poor tracer of synchrotron emission at microwave frequencies, because of the similarity of the thermal dust and synchrotron morphologies. The "after" template removal maps shown here represent the residual contamination present in the *WMAP* CMB cosmological analyses. Higher noise in the ecliptic plane is evident.

because of their complicated noise and signal correlations.

We conclude that *template fits are a valuable method for reducing foreground contamination from CMB maps, but are a poor way to distinguish individual physical emission components due to their correlated morphological structures.*

7. EXTRAGALACTIC SOURCES

In addition to the Galactic foregrounds, extragalactic point sources will contaminate the *WMAP* anisotropy data. Estimates of the level of point source contamination expected at the *WMAP* frequencies have been made based on extrapolations from measured counts at higher and lower frequencies (Park et al. 2002; Sokasian et al. 2001; Refregier et al. 2000; Toffolatti et al. 1998). Direct 15 GHz source count measurements by Taylor et al. (2001) indicate that these extrapolated source counts underestimate the true counts by a factor of two. This is because flatter spectrum synchrotron components increasingly dominate over steeper spectrum components with increasing frequency, as in the case of Galactic emission discussed above. Microwave/millimeter wave observations preferentially sample flat spectrum sources. Techniques that remove Galactic signal contamination, such as the ones described above, will also generally reduce extragalactic contamination. For both Galactic and extragalactic contamination, the most affected *WMAP* pixels should be masked and not used for cosmological purposes. After applying a point source and Galactic signal minimization technique and masking the most contaminated pixels, the residual contribution must be accounted for as a systematic error for CMB analyses.

We examine the point source content of the *WMAP* maps by constructing a catalog of sources surveyed at 4.85 GHz using the northern celestial hemisphere GB6 (Gregory et al. 1996) catalog and the southern hemisphere PMN catalog (Griffith et al. 1994, 1995; Wright et al. 1994, 1996). The GB6 catalog covers $0^\circ < \delta < +75^\circ$ to a flux limit of 18 mJy and the PMN catalog covers $-87^\circ < \delta < +10^\circ$ to a flux limit between 20 and 72 mJy. Combined, these catalogs contain 119,619 sources, with 93,799 in the region $|b| > 10^\circ$. We examined the *WMAP* pixel location for each of these sources as a function of their 4.85 GHz flux density. We find that the detected sources are primarily flat-spectrum, with $\alpha \sim 0$. We also considered the 15,411 IRAS objects in the infrared PSCz catalog (Saunders et al. 2000), but found no significant signal in the *WMAP* data. The detected sources tend to be radio galaxies and quasars, not normal galaxies, so the tight infrared-radio correlation of galaxies discussed in §3.3 is not relevant.

A catalog can be made of the brightest point sources in the *WMAP* maps, independent of their presence in external surveys. First, the temperature maps are weighted by the square-root of the number of observations, $N_{obs}^{1/2}$. The maps are then filtered by $b_l/(b_l^2 C_l^{\rm cmb} + C^{\rm noise})$, (Tegmark & de Oliveira-Costa 1998; Refregier et al. 2000), where b_l is the transfer function of the *WMAP* beam pattern (Page et al. 2003a), $C_l^{\rm cmb}$ is the CMB angular power spectrum, and $C^{\rm noise}$ is the noise power. Peaks that are $>5\sigma$ in the filtered maps are fit to a Gaussian profile plus a baseline plane. This procedure results in 208 point source candidates, listed in Table 5. We cross-correlated this catalog with the GB6, PMN, and Kühr catalogs, identifying sources if they are separated by less than $11'$ (the position uncertainty is $4'$). When more than one source lay within the cutoff radius the brightest one was chosen, and the source flagged. Of the 208 sources in the catalog, 203 sources have counterparts, 20 having more than one. Since the five without counterparts are all near the detection threshold, and simulations suggest that we should expect 5 ± 4 false detections, these are likely spurious. Thus, there is no evidence for a population of bright microwave sources without known radio counterparts.

The sources observed at *WMAP* frequencies are predominately flat-spectrum (Figure 12), with an average spectral index of $\alpha \sim 0$. Modeling the source count distribution dN/dS as a power law $\kappa(S/{\rm Jy})^\beta$, we obtain the values presented in Table 4. We find the slopes to be nearly Euclidean, consistent with the Toffolatti et al. (1998) model (hereafter

referred to as T98), which predicts a steepening in the spectrum at fluxes greater than 1 Jy (Figure 13). T98 appears to overpredict the number of point sources; to fit the Q-band data their model should be rescaled by 0.66 ± 0.06. Independent empirical estimates of the source count at 90 GHz are a factor of two below the T98 prediction (Sokasian et al. 2001; Holdaway et al. 1994).

Given a model for the source count distribution, we can predict the level of residual contamination due to unresolved point sources. The contribution to the anisotropy for Poisson-distributed sources is an effective white-noise term

$$C^{\rm src} = g(\nu)^2 \int_0^{S_c} dS \frac{dN}{dS} S^2 \quad \mu{\rm K}^2{\rm sr} \tag{11}$$

where S_c is the flux limit and $g(\nu) = \left(c^2/2k\nu^2\right)\left((e^x-1)^2/x^2e^x\right)$ converts flux density to thermodynamic temperature (with x defined in §1). Note that point sources are constant in $C^{\rm src}$ and therefore have an l^2 dependence in $l(l+1)C_l/2\pi$. As the point source mask is an amalgam of incomplete catalogs it's difficult to estimate S_c. Primarily constructed from a selection of sources greater than 1 Jy at 5 GHz and 0.5 Jy at 22 GHz, a "split-the-difference" estimate of 0.75 Jy seems reasonable. This value is also suggested by measurements of the bispectrum (Komatsu et al. 2003). Integrating the rescaled T98 model with $S_c = 0.75$ gives us $C^{\rm src} = 35.4 \pm 3.2\, g(\nu)^2$ Jy^{2}sr^{-1}, or $(15.0 \pm 1.4) \times 10^{-3}\mu$K^{2}sr for Q-band. Extrapolating, this implies nearly negligible contamination levels of 3 and $1 \times 10^{-3}\mu$K^{2}sr for V- and W-band.

8. SUNYAEV-ZELDOVICH (SZ) EFFECT

Hot gas in clusters of galaxies will contaminate the maps by shifting the spectrum of the primary anisotropy to create a Sunyaev-Zeldovich decrement in the *WMAP* frequency bands. This is, however, a small effect for *WMAP*.

The brightest SZ source is the Coma cluster, which is included in the point source mask described in §2. The Coma decrement observed by *WMAP* is -0.34 ± 0.18 mK in W-band and -0.24 ± 0.18 mK in V-band.

More generally, the XBACs catalog of 242 Abell-type clusters (Ebeling et al. 1996) is correlated with the *WMAP* W-band map. The XBACs clusters are treated as point sources for *WMAP* and the conversion to units of flux density is based on Refregier et al. (2000), using the relation

$$S_{94} = 11.44 \left(\frac{300\,{\rm Mpc}}{D(z)}\right)^2 \left(\frac{f_{\rm gas}}{0.11}\right) \left(\frac{kT_e}{1\,{\rm keV}}\right)^{5/2} \quad [{\rm mJy}] \tag{12}$$

where $D(z)$ is the angular diameter distance to the cluster, $f_{\rm gas} \equiv M_{\rm gas}/M$ is the gas mass fraction, and T_e is the electron temperature. The overall normalization of this relation is uncertain due to ignorance of the correct gas fraction and cluster virialization state. We fix $f_{\rm gas} = 0.11$. Extended clusters (more than one-third the extent of Coma) are omitted; the remaining fluxes are all < 1 Jy. A template map is constructed by convolving the clusters with the *WMAP* beam (Page et al. 2003a), and then the template is fit to the *WMAP* W-band map. We find a template normalization of -0.36 ± 0.14. Since the fluxes used to construct the template were positive, the negative scaling is consistent with observing the SZ effect at 2.5σ using a matched filter (the X-ray catalog).

CMB photons that travel to us through the plane of our own Galaxy undergo an SZ distortion of $y \approx kn_eT_e\sigma_T L/m_ec^2$, where σ_T is the Thomson scattering cross-section and L is the effective (electron pressure weighted) length of the path through our Galaxy. Taking $n_eT_e = 10^3$ K cm^{-3} and $L = 50$ kpc we get $y \approx 2 \times 10^{-8}$. Therefore our Galaxy does not significantly affect the CMB photons, even in the worst case. More generally, the SZ effect, as a contaminating foreground, can safely be ignored for *WMAP* data analyses.

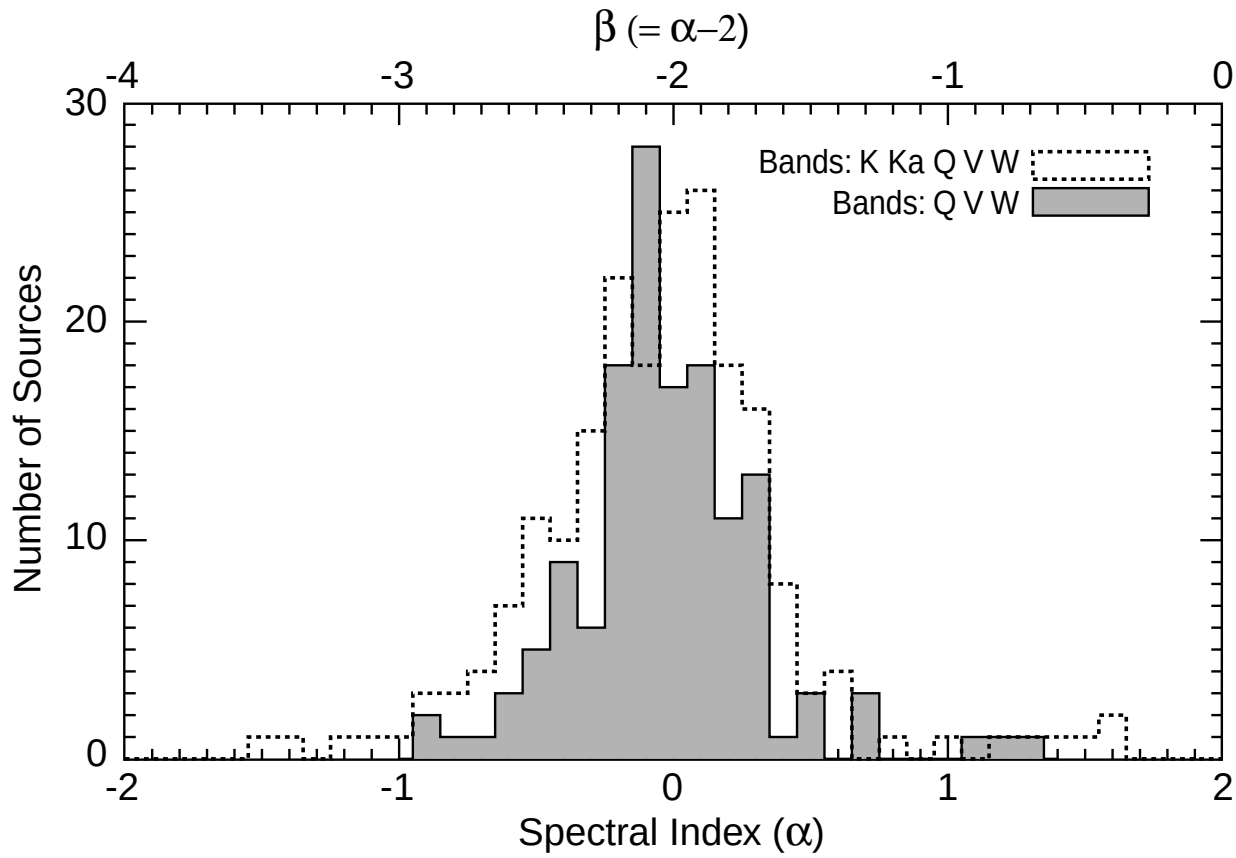

Fig. 12.— A spectral index histogram of the 208 point sources detected by *WMAP*. The mean spectral index is $\alpha = 0$ ($\beta = -2$).

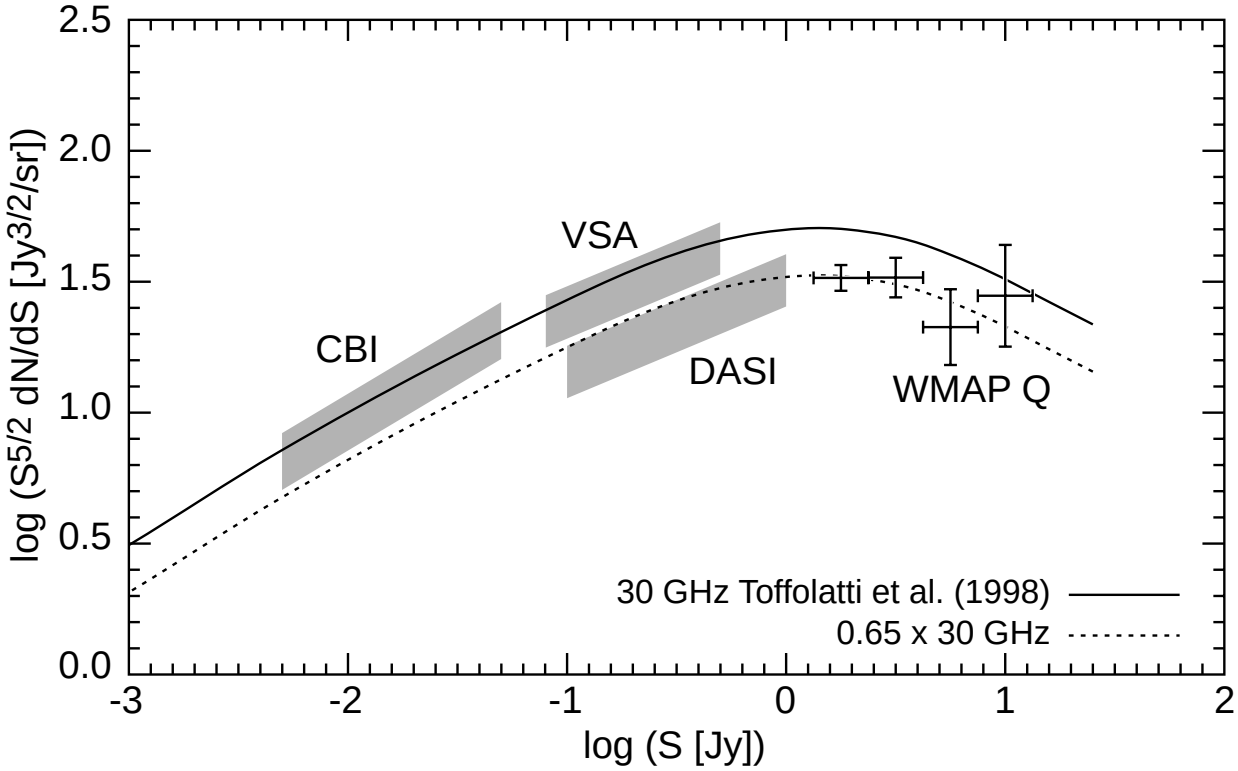

Fig. 13.— Point source counts derived from *WMAP* compared with other independent measurements and the Toffolatti et al. (1998) 30 GHz model. The VSA measurement of dN/dS was made at 15 GHz (Taylor et al. 2002). whereas CBI (Mason et al. 2002) & DASI (Halverson et al. 2002) measurements were made at 31 GHz. The boxes indicate the 1σ normalization uncertainty bounds, ignoring the slope uncertainty.

Table 5. MAP Source Catalog

	l [°]	b [°]	K [Jy]	Ka [Jy]	Q [Jy]	V [Jy]	W [Jy]	α	5 GHz ID	
001	0.59	–42.88	1.5 ± 0.1	1.8 ± 0.2	1.4 ± 0.3	1.0 ± 0.3	···	-0.0 ± 0.5	PMN J2109-4110	
002	1.31	45.99	1.8 ± 0.1	2.2 ± 0.2	1.6 ± 0.2	1.1 ± 0.4	···	-0.0 ± 0.4	GB6 J1516+0015	
003	1.58	–28.97	3.2 ± 0.1	3.7 ± 0.2	2.9 ± 0.2	2.6 ± 0.4	2.8 ± 0.7	-0.1 ± 0.2	PMN J1957-3845	
004	8.95	73.13	1.3 ± 0.1	1.5 ± 0.2	1.3 ± 0.2	···	···	0.0 ± 0.7	GB6 J1357+1919	
005	10.85	40.92	1.9 ± 0.1	1.9 ± 0.2	1.7 ± 0.3	1.6 ± 0.6	···	-0.1 ± 0.5	GB6 J1549+0237	
006	11.38	54.54	2.1 ± 0.1	2.1 ± 0.2	2.2 ± 0.2	···	···	0.1 ± 0.4	GB6 J1504+1029	
007	14.22	42.20	2.3 ± 0.1	2.2 ± 0.2	1.8 ± 0.2	1.9 ± 0.5	···	-0.2 ± 0.4	GB6 J1550+0527	
008	17.14	–16.25	2.4 ± 0.1	2.5 ± 0.2	2.3 ± 0.2	···	···	0.0 ± 0.4	PMN J1923-2104	
009	23.01	40.76	3.2 ± 0.1	3.3 ± 0.2	2.7 ± 0.2	3.1 ± 0.5	3.1 ± 0.8	-0.1 ± 0.2	GB6 J1608+1029	
010	23.08	28.93	1.1 ± 0.1	0.7 ± 0.2	···	···	···	-1.4 ± 2	GB6 J1651+0459	
011	24.00	–23.13	1.5 ± 0.1	1.2 ± 0.3	1.3 ± 0.2	1.7 ± 0.3	···	0.0 ± 0.5	PMN J2000-1748	
012	24.41	–64.92	9.6 ± 0.1	9.8 ± 0.2	9.8 ± 0.2	8.9 ± 0.5	6.3 ± 0.8	-0.0 ± 0.08	PMN J2258-2758	
013	26.71	28.71	1.3 ± 0.1	1.3 ± 0.2	1.2 ± 0.2	···	···	-0.1 ± 0.7	GB6 J1658+0741	
014	27.04	–24.61	···	0.7 ± 0.2	···	1.8 ± 0.6	···	1.6 ± 2	PMN J2011-1546	
015	32.73	–29.65	0.7 ± 0.2	···	1.0 ± 0.2	···	···	0.5 ± 1	···	
016	36.61	–51.20	1.9 ± 0.1	1.2 ± 0.2	1.9 ± 0.3	1.6 ± 0.6	···	-0.3 ± 0.5	PMN J2206-1835	
017	40.54	–40.95	3.2 ± 0.1	2.7 ± 0.2	2.9 ± 0.2	2.0 ± 0.4	···	-0.3 ± 0.3	PMN J2131-1207	
018	40.61	–48.05	2.1 ± 0.1	2.3 ± 0.2	2.1 ± 0.3	2.1 ± 0.6	···	0.0 ± 0.4	PMN J2158-1501	
019	41.54	–62.81	1.2 ± 0.2	1.3 ± 0.2	···	1.9 ± 0.8	···	0.3 ± 0.8	PMN J2256-2011	
020	52.32	–36.49	1.7 ± 0.1	1.7 ± 0.2	1.6 ± 0.3	1.4 ± 0.5	2.0 ± 0.6	-0.0 ± 0.4	PMN J2134-0153	
021	53.78	–57.10	1.6 ± 0.1	1.4 ± 0.3	1.5 ± 0.4	···	···	-0.2 ± 0.8	PMN J2246-1206	
022	54.15	24.49	2.1 ± 0.09	2.2 ± 0.2	2.7 ± 0.2	3.2 ± 0.4	2.2 ± 0.7	0.3 ± 0.2	GB6 J1753+2847	
023	55.14	46.37	3.5 ± 0.1	2.8 ± 0.2	2.9 ± 0.2	2.0 ± 0.4	1.4 ± 0.5	-0.5 ± 0.2	GB6 J1613+3412	
024	55.21	–51.70	1.5 ± 0.1	1.9 ± 0.2	2.2 ± 0.3	2.2 ± 0.3	···	0.4 ± 0.4	PMN J2229-0832	
025	55.48	–35.57	4.2 ± 0.1	3.6 ± 0.2	3.2 ± 0.3	2.3 ± 0.5	···	-0.5 ± 0.3	GB6 J2136+0041	
026	56.47	80.64	2.1 ± 0.1	2.1 ± 0.2	1.3 ± 0.2	···	···	-0.5 ± 0.5	GB6 J1331+3030	
027	58.00	–30.11	2.1 ± 0.1	1.7 ± 0.2	2.0 ± 0.3	···	2.1 ± 0.8	-0.1 ± 0.4	GB6 J2123+0535	
028	58.57	12.64	1.4 ± 0.08	1.1 ± 0.1	0.9 ± 0.1	···	···	-0.6 ± 0.5	GB6 J1850+2825	
029	58.97	–48.84	6.4 ± 0.1	6.1 ± 0.2	5.7 ± 0.3	4.8 ± 0.5	7.1 ± 3	-0.2 ± 0.1	PMN J2225-0457	
030	59.03	–46.63	2.5 ± 0.1	1.8 ± 0.2	1.8 ± 0.3	···	···	-0.7 ± 0.6	PMN J2218-0335	
031	59.31	–11.63	1.0 ± 0.1	1.6 ± 0.2	···	···	···	1.2 ± 0.9	GB6 J2024+1718	
032	59.85	–68.32	1.5 ± 0.1	···	1.5 ± 0.3	···	1.9 ± 0.6	0.2 ± 0.5	PMN J2331-1556	
033	61.08	42.33	4.6 ± 0.1	5.6 ± 0.2	6.0 ± 0.2	5.9 ± 0.3	4.2 ± 0.7	0.3 ± 0.1	GB6 J1635+3808	
034	62.93	11.65	1.3 ± 0.09	1.3 ± 0.2	0.8 ± 0.1	0.9 ± 0.4	···	-0.5 ± 0.6	GB6 J1902+3159	
035	63.45	40.96	8.0 ± 0.1	7.4 ± 0.2	6.8 ± 0.2	5.8 ± 0.4	5.7 ± 0.7	-0.3 ± 0.09	GB6 J1642+3948	
036	63.45	38.78	1.2 ± 0.09	1.4 ± 0.2	0.5 ± 0.2	···	···	-0.1 ± 0.8	GB6 J1653+3945	*
037	63.66	–34.07	8.6 ± 0.1	8.2 ± 0.2	8.1 ± 0.3	6.1 ± 0.4	···	-0.2 ± 0.1	GB6 J2148+0657	
038	63.91	31.02	1.1 ± 0.1	···	1.4 ± 0.2	1.1 ± 0.4	···	0.2 ± 0.5	GB6 J1734+3857	
039	65.57	–71.92	2.0 ± 0.1	2.1 ± 0.2	2.3 ± 0.2	2.1 ± 0.7	2.3 ± 0.7	0.1 ± 0.3	PMN J2348-1631	
040	65.30	80.35	1.1 ± 0.1	1.4 ± 0.3	1.4 ± 0.6	···	···	0.5 ± 1	GB6 J1329+3154	
041	68.60	–27.57	2.6 ± 0.1	2.4 ± 0.2	1.9 ± 0.2	1.7 ± 0.3	1.5 ± 0.8	-0.4 ± 0.3	GB6 J2139+1423	
042	69.83	68.37	···	1.2 ± 0.1	1.3 ± 0.2	1.6 ± 0.3	1.5 ± 0.5	0.3 ± 0.7	GB6 J1419+3822	
043	71.44	33.30	1.7 ± 0.1	2.0 ± 0.2	1.4 ± 0.2	2.0 ± 0.3	1.6 ± 0.5	0.0 ± 0.3	GB6 J1727+4530	
044	72.02	–26.11	1.3 ± 0.1	1.4 ± 0.2	···	2.0 ± 0.8	1.2 ± 0.6	0.1 ± 0.6	GB6 J2143+1743	
045	75.60	–29.66	1.2 ± 0.1	1.3 ± 0.2	1.4 ± 0.2	0.9 ± 0.3	···	0.0 ± 0.5	GB6 J2203+1725	
046	77.25	23.49	2.6 ± 0.1	2.6 ± 0.2	2.3 ± 0.2	1.5 ± 0.2	1.7 ± 0.4	-0.3 ± 0.2	GB6 J1829+4844	
047	77.47	–38.57	3.6 ± 0.1	3.5 ± 0.2	3.7 ± 0.3	3.6 ± 0.4	3.1 ± 0.7	-0.0 ± 0.2	GB6 J2232+1143	
048	79.57	31.77	1.1 ± 0.1	1.1 ± 0.1	0.4 ± 0.2	1.8 ± 0.4	···	0.2 ± 0.5	GB6 J1740+5211	
049	80.36	–8.35	···	1.3 ± 0.2	0.9 ± 0.2	1.4 ± 0.3	1.7 ± 0.6	0.3 ± 0.7	GB6 J2109+3532	*

Table 5—Continued

	l [°]	b [°]	K [Jy]	Ka [Jy]	Q [Jy]	V [Jy]	W [Jy]	α	5 GHz ID	
050	82.11	–26.09	1.3 ± 0.1	···	1.7 ± 0.2	1.3 ± 0.6	···	0.3 ± 0.5	GB6 J2212+2355	
051	85.34	11.82	0.5 ± 0.09	1.2 ± 0.2	1.2 ± 0.2	···	···	1.5 ± 0.9	GB6 J1955+5131	
052	85.67	83.32	2.6 ± 0.1	2.5 ± 0.2	2.6 ± 0.2	2.2 ± 0.4	···	-0.1 ± 0.3	GB6 J1310+3220	
053	85.73	26.04	1.4 ± 0.09	1.3 ± 0.2	1.5 ± 0.2	···	···	0.1 ± 0.5	GB6 J1824+5650	
054	85.96	–18.76	3.5 ± 0.1	3.3 ± 0.2	3.0 ± 0.2	2.4 ± 0.4	3.7 ± 0.8	-0.2 ± 0.2	GB6 J2203+3145	
055	86.13	–38.19	7.5 ± 0.1	7.1 ± 0.2	6.9 ± 0.2	5.9 ± 0.4	5.9 ± 0.9	-0.2 ± 0.1	GB6 J2253+1608	
056	86.73	40.33	···	1.7 ± 0.2	1.1 ± 0.1	1.3 ± 0.2	···	-0.5 ± 0.8	GB6 J1638+5720	
057	90.07	–25.65	1.4 ± 0.1	1.9 ± 0.2	1.3 ± 0.2	···	···	0.2 ± 0.6	GB6 J2236+2828	
058	92.62	–10.44	3.1 ± 0.1	2.9 ± 0.2	3.3 ± 0.2	···	···	0.1 ± 0.2	GB6 J2202+4216	
059	92.74	19.45	···	1.0 ± 0.2	1.4 ± 0.2	1.2 ± 0.3	1.2 ± 0.6	0.2 ± 0.8	GB6 J1927+6117	
060	93.45	–66.61	2.0 ± 0.2	2.1 ± 0.3	1.9 ± 0.3	2.0 ± 0.4	···	0.0 ± 0.4	PMN J0006-0623	*
061	96.01	–11.23	2.2 ± 0.5	1.4 ± 0.3	···	···	···	-1.2 ± 2	···	
062	96.87	–87.87	1.3 ± 0.1	0.4 ± 0.2	1.3 ± 0.3	1.9 ± 0.6	···	0.2 ± 0.6	PMN J0047-2517	
063	96.09	13.72	1.7 ± 0.1	1.5 ± 0.2	1.4 ± 0.2	1.3 ± 0.3	···	-0.3 ± 0.4	GB6 J2022+6137	
064	96.33	29.90	0.6 ± 0.04	0.6 ± 0.05	0.5 ± 0.1	0.5 ± 0.2	···	-0.2 ± 0.5	GB6 J1758+6638	*
065	97.50	25.00	1.2 ± 0.08	1.4 ± 0.1	1.6 ± 0.1	1.1 ± 0.2	1.4 ± 0.4	0.1 ± 0.3	GB6 J1849+6705	*
066	98.48	25.81	···	1.1 ± 0.1	1.1 ± 0.1	···	···	0.3 ± 2	GB6 J1842+6809	
067	100.13	29.17	1.3 ± 0.07	1.1 ± 0.1	1.2 ± 0.1	1.5 ± 0.3	···	-0.0 ± 0.3	GB6 J1806+6949	
068	100.54	30.69	0.6 ± 0.09	2.0 ± 0.8	1.0 ± 0.1	1.5 ± 0.3	···	0.8 ± 0.5	GB6 J1748+7005	
069	100.59	36.63	1.2 ± 0.1	0.9 ± 0.2	0.9 ± 0.2	···	···	-0.5 ± 0.8	GB6 J1642+6856	*
070	105.62	23.55	3.7 ± 0.09	3.8 ± 0.1	3.2 ± 0.1	3.5 ± 0.3	···	-0.1 ± 0.1	GB6 J1927+7357	
071	110.04	42.11	1.6 ± 0.1	1.4 ± 0.2	1.5 ± 0.2	1.2 ± 0.5	···	-0.2 ± 0.5	GB6 J1459+7140	
072	110.04	29.09	2.3 ± 0.1	1.8 ± 0.1	2.3 ± 0.2	1.5 ± 0.3	···	-0.2 ± 0.3	1Jy 1803+78	
073	111.41	27.14	1.3 ± 0.09	1.0 ± 0.2	···	···	···	-0.7 ± 1	1Jy 1845+79	
074	112.64	–15.89	1.8 ± 0.1	···	1.7 ± 0.3	1.8 ± 0.6	···	-0.1 ± 0.5	GB6 J2354+4553	
075	113.92	–12.04	1.0 ± 0.08	0.9 ± 0.1	···	···	···	-0.2 ± 0.9	···	
076	115.66	31.23	1.2 ± 0.09	1.5 ± 0.1	1.0 ± 0.1	1.2 ± 0.3	···	0.1 ± 0.4	···	
077	122.77	–72.30	1.3 ± 0.1	1.4 ± 0.2	···	···	···	0.1 ± 1	PMN J0050-0928	
078	125.71	35.79	···	···	0.6 ± 0.2	1.5 ± 0.6	···	2.5 ± 3	1Jy 1150+81	
079	129.26	–49.33	1.4 ± 0.1	1.6 ± 0.3	···	···	···	0.4 ± 1	GB6 J0108+1319	
080	130.79	–14.29	4.5 ± 0.1	4.7 ± 0.2	4.2 ± 0.2	3.3 ± 0.4	2.9 ± 0.7	-0.2 ± 0.2	GB6 J0136+4751	
081	131.83	–60.97	2.1 ± 0.1	2.3 ± 0.2	2.3 ± 0.3	2.5 ± 0.4	···	0.2 ± 0.3	GB6 J0108+0135	*
082	133.46	18.38	1.0 ± 0.1	···	0.6 ± 0.2	0.9 ± 0.4	···	-0.4 ± 0.8	1Jy 0403+76	
083	135.56	42.27	1.1 ± 0.1	1.5 ± 0.3	1.1 ± 0.3	1.4 ± 0.5	···	0.2 ± 0.7	GB6 J1048+7143	
084	140.19	–16.72	2.1 ± 0.1	···	1.3 ± 0.3	1.3 ± 0.4	1.8 ± 0.7	-0.4 ± 0.4	GB6 J0223+4259	*
085	140.50	–28.14	1.5 ± 0.2	1.8 ± 0.3	1.3 ± 0.4	···	···	0.1 ± 1	GB6 J0205+3212	
086	141.17	–61.85	1.3 ± 0.1	1.7 ± 0.2	1.4 ± 0.3	1.8 ± 0.4	···	0.3 ± 0.5	PMN J0125-0005	*
087	141.27	25.11	0.8 ± 0.1	0.8 ± 0.2	1.1 ± 0.2	···	···	0.4 ± 0.8	GB6 J0639+7324	
088	141.53	40.59	1.4 ± 0.1	1.3 ± 0.2	1.3 ± 0.2	···	···	-0.2 ± 0.7	GB6 J0955+6940	
089	143.48	34.43	1.5 ± 0.1	···	1.2 ± 0.2	1.4 ± 0.4	···	-0.2 ± 0.5	GB6 J0841+7053	
090	145.59	64.97	1.8 ± 0.09	···	1.8 ± 0.2	1.6 ± 0.4	1.3 ± 0.6	-0.1 ± 0.4	GB6 J1153+4931	*
091	146.82	20.78	1.2 ± 0.08	1.2 ± 0.1	1.3 ± 0.4	1.3 ± 0.4	···	0.1 ± 0.5	GB6 J0607+6720	
092	147.92	–44.04	1.7 ± 0.2	1.6 ± 0.3	1.8 ± 0.2	···	···	0.0 ± 0.6	GB6 J0204+1514	
093	149.49	–28.52	3.9 ± 0.1	4.0 ± 0.2	3.9 ± 0.3	1.8 ± 0.4	···	-0.2 ± 0.3	GB6 J0237+2848	
094	150.56	–13.26	11.1 ± 0.1	8.7 ± 0.2	6.9 ± 0.3	4.7 ± 0.4	···	-0.8 ± 0.1	GB6 J0319+4130	
095	161.69	10.31	1.6 ± 0.2	1.4 ± 0.3	···	···	···	-0.5 ± 1	GB6 J0542+4951	
096	162.36	–54.39	1.6 ± 0.1	3.4 ± 2	1.6 ± 0.2	···	···	0.1 ± 0.5	GB6 J0217+0144	
097	167.92	–76.02	0.6 ± 0.1	1.6 ± 0.2	1.9 ± 0.2	1.6 ± 0.6	···	1.4 ± 0.7	PMN J0132-1654	
098	170.20	50.71	1.7 ± 0.1	1.7 ± 0.2	1.2 ± 0.2	···	···	-0.4 ± 0.6	GB6 J0958+4725	

Table 5—Continued

	l [°]	b [°]	K [Jy]	Ka [Jy]	Q [Jy]	V [Jy]	W [Jy]	α	5 GHz ID	
099	171.12	17.94	3.2 ± 0.1	2.4 ± 0.2	2.5 ± 0.3	2.3 ± 0.5	1.7 ± 0.8	-0.5 ± 0.3	GB6 J0646+4451	
100	171.73	7.30	1.2 ± 0.2	2.2 ± 0.2	···	···	···	1.6 ± 1	GB6 J0555+3948	
101	174.65	69.79	1.3 ± 0.1	1.0 ± 0.2	1.6 ± 0.4	···	···	-0.1 ± 0.8	GB6 J1130+3815	*
102	174.96	–44.53	1.5 ± 0.2	1.2 ± 0.2	1.2 ± 0.2	1.0 ± 0.4	···	-0.4 ± 0.6	GB6 J0308+0406	
103	177.42	58.33	1.5 ± 0.1	1.7 ± 0.2	1.5 ± 0.3	···	2.6 ± 0.9	0.2 ± 0.4	GB6 J1033+4115	
104	181.05	50.30	1.5 ± 0.1	1.8 ± 0.2	1.8 ± 0.2	2.0 ± 0.4	···	0.3 ± 0.4	GB6 J0948+4039	
105	183.72	46.16	6.8 ± 0.1	5.8 ± 0.2	5.5 ± 0.2	5.1 ± 0.5	3.1 ± 0.8	-0.4 ± 0.1	GB6 J0927+3902	
106	187.97	–42.46	2.8 ± 0.2	2.8 ± 0.3	3.1 ± 0.3	3.0 ± 0.7	3.2 ± 0.8	0.1 ± 0.3	PMN J0339-0146	
107	188.62	23.62	1.6 ± 0.1	0.8 ± 0.2	···	2.3 ± 0.9	2.2 ± 1	0.0 ± 0.5	GB6 J0741+3112	
108	190.39	–27.38	2.2 ± 0.1	2.4 ± 0.2	1.9 ± 0.3	1.8 ± 0.6	3.0 ± 1	0.0 ± 0.4	GB6 J0433+0521	
109	193.60	–31.74	1.6 ± 0.2	2.1 ± 0.2	1.9 ± 0.2	···	···	0.4 ± 0.6	GB6 J0424+0036	
110	195.30	–33.13	7.4 ± 0.1	7.3 ± 0.2	7.0 ± 0.3	6.8 ± 0.5	3.9 ± 1	-0.1 ± 0.1	PMN J0423-0120	
111	199.35	78.38	3.5 ± 0.1	3.6 ± 0.2	3.4 ± 0.2	3.0 ± 0.4	2.1 ± 0.6	-0.1 ± 0.2	GB6 J1159+2914	
112	200.07	31.86	1.7 ± 0.2	1.6 ± 0.2	2.4 ± 0.4	3.1 ± 0.7	···	0.5 ± 0.5	GB6 J0830+2410	
113	201.73	18.16	1.5 ± 0.1	···	1.5 ± 0.3	···	···	0.1 ± 0.7	GB6 J0738+1742	
114	205.62	–42.60	4.8 ± 1	1.6 ± 0.2	1.6 ± 0.2	1.3 ± 0.4	···	-1.0 ± 0.8	PMN J0405-1308	
115	206.82	35.80	2.6 ± 0.2	3.5 ± 0.3	2.9 ± 0.3	2.5 ± 0.5	2.5 ± 0.8	0.1 ± 0.3	GB6 J0854+2006	
116	207.39	–23.18	···	···	1.7 ± 0.2	···	1.8 ± 0.8	0.0 ± 1	···	
117	208.20	18.76	2.3 ± 0.2	2.0 ± 0.2	2.1 ± 0.3	2.1 ± 0.5	···	-0.2 ± 0.4	GB6 J0750+1231	
118	209.74	16.58	1.4 ± 0.2	···	0.9 ± 0.2	···	···	-0.9 ± 1	GB6 J0745+1011	
119	210.55	54.30	1.7 ± 0.1	1.5 ± 0.2	···	···	···	-0.3 ± 1	GB6 J1014+2301	
120	211.25	19.14	···	1.7 ± 0.3	1.2 ± 0.2	···	···	-1.5 ± 3	GB6 J0757+0956	
121	212.96	30.09	1.6 ± 0.2	2.1 ± 0.3	···	···	···	0.6 ± 1	GB6 J0840+1312	
122	215.23	–24.23	1.4 ± 0.1	1.9 ± 0.2	1.4 ± 0.2	···	···	0.3 ± 0.6	PMN J0527-1241	
123	216.70	–54.26	1.0 ± 0.09	1.5 ± 0.2	1.2 ± 0.2	1.0 ± 0.3	···	0.3 ± 0.6	PMN J0329-2357	*
124	217.01	11.36	1.8 ± 0.1	1.8 ± 0.2	1.9 ± 0.3	2.3 ± 0.5	1.5 ± 0.7	0.1 ± 0.4	GB6 J0739+0136	
125	221.13	22.37	1.4 ± 0.1	1.7 ± 0.2	1.1 ± 0.3	2.0 ± 0.5	···	0.2 ± 0.5	GB6 J0825+0309	
126	222.59	–16.18	3.9 ± 0.1	3.3 ± 0.2	3.9 ± 0.3	2.0 ± 0.4	···	-0.3 ± 0.2	PMN J0609-1542	
127	223.45	–30.67	1.1 ± 0.09	1.0 ± 0.1	1.4 ± 0.4	···	···	0.1 ± 0.8	PMN J0513-2159	
128	223.67	–34.89	3.3 ± 0.09	3.8 ± 0.2	3.8 ± 0.2	3.5 ± 0.5	2.7 ± 0.6	0.2 ± 0.2	PMN J0457-2324	
129	224.51	–50.79	1.4 ± 0.08	1.2 ± 0.1	1.0 ± 0.1	···	···	-0.6 ± 0.5	PMN J0348-2749	
130	228.66	–13.61	1.3 ± 0.1	1.3 ± 0.2	1.3 ± 0.2	···	···	0.1 ± 0.6	PMN J0629-1959	
131	229.01	–36.96	1.7 ± 0.1	1.9 ± 0.2	7.6 ± 3	···	···	0.6 ± 0.7	PMN J0453-2807	
132	229.00	30.93	2.2 ± 0.1	2.1 ± 0.2	2.2 ± 0.3	0.8 ± 0.4	···	-0.2 ± 0.5	GB6 J0909+0121	
133	229.04	13.16	1.3 ± 0.1	1.4 ± 0.2	1.4 ± 0.2	2.2 ± 0.4	1.2 ± 0.6	0.3 ± 0.4	PMN J0808-0751	
134	229.84	–12.38	1.2 ± 0.1	0.3 ± 0.1	1.2 ± 0.2	···	···	-0.2 ± 0.6	PMN J0636-2041	*
135	231.22	–13.70	0.9 ± 0.1	0.9 ± 0.1	1.5 ± 0.2	···	1.7 ± 0.5	0.6 ± 0.5	PMN J0633-2223	
136	237.74	–48.48	2.7 ± 0.1	2.9 ± 0.2	2.5 ± 0.2	2.6 ± 0.3	2.1 ± 0.5	-0.1 ± 0.2	PMN J0403-3605	
137	239.76	–69.07	0.9 ± 0.07	1.0 ± 0.1	···	0.8 ± 0.3	1.1 ± 0.4	0.1 ± 0.5	PMN J0222-3441	
138	240.11	–56.89	···	···	···	1.9 ± 0.3	1.4 ± 0.5	-0.8 ± 2	PMN J0321-3711	*
139	240.61	–32.72	3.9 ± 0.1	3.4 ± 0.2	3.2 ± 0.2	2.8 ± 0.4	2.3 ± 0.6	-0.4 ± 0.2	PMN J0522-3628	
140	240.71	–44.43	1.3 ± 0.1	···	1.1 ± 0.2	1.1 ± 0.4	···	-0.2 ± 0.6	PMN J0424-3756	
141	241.23	–47.90	1.0 ± 0.1	1.5 ± 0.2	1.3 ± 0.2	1.0 ± 0.3	···	0.3 ± 0.6	PMN J0406-3826	
142	241.72	51.54	1.8 ± 0.2	1.8 ± 0.3	1.4 ± 0.3	1.9 ± 0.5	···	-0.1 ± 0.5	GB6 J1038+0512	
143	242.86	25.11	2.0 ± 0.1	···	0.8 ± 0.3	···	1.4 ± 0.7	-0.5 ± 0.7	PMN J0918-1205	
144	243.56	12.26	3.3 ± 0.1	2.9 ± 0.2	3.0 ± 0.2	2.1 ± 0.3	···	-0.3 ± 0.2	PMN J0836-2017	
145	244.36	6.05	1.1 ± 0.09	1.4 ± 0.2	1.7 ± 0.2	2.0 ± 0.4	···	0.6 ± 0.4	PMN J0816-2421	
146	244.72	–54.06	1.7 ± 0.1	1.7 ± 0.2	1.7 ± 0.2	2.0 ± 0.4	2.2 ± 0.8	0.1 ± 0.3	PMN J0334-4008	
147	248.42	–41.55	3.4 ± 0.1	3.7 ± 0.2	3.4 ± 0.2	2.5 ± 0.3	2.5 ± 0.7	-0.1 ± 0.2	PMN J0440-4332	

Table 5—Continued

	l [°]	b [°]	K [Jy]	Ka [Jy]	Q [Jy]	V [Jy]	W [Jy]	α	5 GHz ID	
148	250.09	–31.08	7.9 ± 0.1	8.2 ± 0.2	8.8 ± 0.2	7.9 ± 0.4	6.7 ± 0.6	0.0 ± 0.07	PMN J0538-4405	
149	251.50	52.77	5.9 ± 0.1	5.7 ± 0.2	6.5 ± 0.3	5.2 ± 0.4	4.6 ± 2	–0.0 ± 0.1	GB6 J1058+0133	
150	251.59	–34.64	6.8 ± 0.1	5.3 ± 0.2	3.9 ± 0.2	2.9 ± 0.3	···	–0.8 ± 0.1	PMN J0519-4546	*
151	251.99	–38.80	3.0 ± 0.1	4.0 ± 0.2	3.7 ± 0.2	3.4 ± 0.4	3.8 ± 0.9	0.3 ± 0.2	PMN J0455-4616	
152	262.01	–31.87	1.3 ± 0.1	1.4 ± 0.2	1.8 ± 0.2	1.6 ± 0.3	···	0.3 ± 0.4	PMN J0540-5418	
153	265.89	–30.67	1.3 ± 0.09	3.1 ± 1	1.2 ± 0.2	···	···	–0.0 ± 0.6	PMN J0550-5732	
154	270.52	–36.04	2.6 ± 0.09	2.4 ± 0.1	2.0 ± 0.2	1.5 ± 0.3	···	–0.4 ± 0.3	PMN J0506-6109	*
155	272.49	–54.59	2.7 ± 0.1	3.1 ± 0.1	3.5 ± 0.2	2.9 ± 0.3	2.2 ± 0.5	0.2 ± 0.2	PMN J0253-5441	
156	273.59	–31.25	0.8 ± 0.06	0.6 ± 0.09	0.6 ± 0.1	···	···	–0.6 ± 0.8	PMN J0546-6415	
157	275.35	43.60	1.9 ± 0.1	1.7 ± 0.2	1.9 ± 0.2	1.4 ± 0.3	···	–0.2 ± 0.4	PMN J1130-1449	
158	276.09	–61.76	3.0 ± 0.1	2.9 ± 0.2	3.0 ± 0.2	3.4 ± 0.4	1.8 ± 0.6	0.0 ± 0.2	PMN J0210-5101	
159	276.76	39.62	···	0.7 ± 0.2	1.2 ± 0.2	1.3 ± 0.5	···	1.0 ± 2	PMN J1127-1857	
160	278.14	–48.90	1.3 ± 0.1	···	···	1.6 ± 0.5	···	0.2 ± 0.8	PMN J0309-6058	
161	279.51	–20.16	1.6 ± 0.1	1.0 ± 0.1	1.0 ± 0.2	···	···	–1.1 ± 0.6	PMN J0743-6726	*
162	280.29	–48.71	1.5 ± 0.1	1.6 ± 0.2	1.5 ± 0.2	1.7 ± 0.3	···	0.1 ± 0.4	PMN J0303-6211	
163	281.44	9.75	1.2 ± 0.1	1.1 ± 0.2	0.5 ± 0.1	···	···	–0.9 ± 1	PMN J1041-4740	
164	281.86	67.35	2.6 ± 0.1	2.1 ± 0.2	1.9 ± 0.2	2.0 ± 0.6	···	–0.5 ± 0.4	GB6 J1219+0549A	*
165	283.81	74.49	19.7 ± 0.1	15.8 ± 0.2	13.1 ± 0.2	9.2 ± 0.4	5.3 ± 0.6	–0.7 ± 0.06	GB6 J1230+1223	
166	284.19	14.25	2.0 ± 0.09	1.7 ± 0.1	1.4 ± 0.1	1.4 ± 0.4	1.7 ± 0.7	–0.4 ± 0.3	PMN J1107-4449	
167	286.39	–27.15	4.6 ± 0.09	4.4 ± 0.1	3.9 ± 0.1	3.6 ± 0.3	···	–0.3 ± 0.1	PMN J0635-7516	
168	288.31	–63.89	···	1.3 ± 0.2	0.5 ± 0.1	···	···	–4.8 ± 4	PMN J0133-5159	
169	289.25	22.95	2.9 ± 0.1	3.3 ± 0.2	2.9 ± 0.2	2.8 ± 0.4	···	0.0 ± 0.2	PMN J1147-3812	
170	289.95	64.36	20.0 ± 0.1	18.3 ± 0.2	17.5 ± 0.3	14.5 ± 0.4	9.0 ± 0.8	–0.3 ± 0.04	GB6 J1229+0202	
171	290.72	–76.16	2.3 ± 0.09	2.4 ± 0.2	1.9 ± 0.2	1.6 ± 0.4	···	–0.2 ± 0.3	PMN J0106-4034	
172	290.54	37.82	1.5 ± 0.1	1.1 ± 0.2	···	···	···	–0.9 ± 1	PMN J1209-2406	
173	291.04	44.52	1.7 ± 0.1	1.6 ± 0.3	1.6 ± 0.3	1.3 ± 0.4	···	–0.2 ± 0.5	PMN J1215-1731	
174	293.30	–37.61	1.0 ± 0.09	1.3 ± 0.1	1.0 ± 0.3	1.3 ± 0.5	···	0.4 ± 0.6	PMN J0311-7651	
175	293.85	–31.40	2.0 ± 0.1	2.2 ± 0.2	1.8 ± 0.1	2.5 ± 0.4	1.6 ± 0.7	0.1 ± 0.3	PMN J0450-8100	
176	298.06	–18.27	2.0 ± 0.1	2.2 ± 0.1	2.4 ± 0.2	2.4 ± 0.3	···	0.2 ± 0.3	PMN J1058-8003	
177	301.63	37.12	1.4 ± 0.2	1.9 ± 0.4	···	1.0 ± 0.4	···	–0.0 ± 0.8	PMN J1246-2547	
178	302.00	–20.33	1.1 ± 0.09	1.6 ± 0.8	1.3 ± 0.1	···	···	0.3 ± 0.5	PMN J1224-8312	
179	303.32	–59.45	1.3 ± 0.1	1.2 ± 0.2	0.7 ± 0.1	1.5 ± 0.4	···	–0.2 ± 0.5	PMN J0050-5738	
180	304.58	30.87	1.7 ± 0.1	1.3 ± 0.2	1.7 ± 0.3	···	···	–0.3 ± 0.6	PMN J1257-3154	
181	305.11	57.06	···	24.9 ± 0.2	···	24.5 ± 0.5	19.0 ± 0.9	–0.1 ± 0.06	PMN J1256-0547	
182	308.79	29.02	1.4 ± 0.1	1.6 ± 0.2	1.7 ± 0.2	1.6 ± 0.4	···	0.2 ± 0.4	PMN J1316-3339	
183	313.45	–18.85	2.4 ± 0.1	2.0 ± 0.1	1.8 ± 0.2	2.0 ± 0.4	···	–0.4 ± 0.3	PMN J1617-7717	
184	313.47	–35.13	1.6 ± 0.09	1.3 ± 0.1	1.0 ± 0.2	···	···	–0.6 ± 0.6	PMN J2146-7755	
185	313.54	27.99	1.7 ± 0.1	1.5 ± 0.2	1.1 ± 0.2	1.7 ± 0.4	···	–0.3 ± 0.5	PMN J1336-3358	
186	313.68	–23.40	1.0 ± 0.1	···	1.0 ± 0.1	···	···	0.0 ± 0.7	PMN J1733-7935	
187	314.12	–55.14	1.8 ± 0.1	···	1.3 ± 0.1	···	···	–0.5 ± 0.5	PMN J2358-6054	
188	320.02	48.37	6.3 ± 0.1	6.7 ± 0.2	7.3 ± 0.3	6.6 ± 0.4	3.7 ± 0.7	0.1 ± 0.1	PMN J1337-1257	
189	320.14	–62.06	···	1.3 ± 0.2	···	1.7 ± 0.6	···	0.4 ± 1	PMN J2357-5311	
190	321.31	–40.64	3.6 ± 0.1	2.9 ± 0.2	2.6 ± 0.2	2.2 ± 0.4	···	–0.6 ± 0.2	PMN J2157-6941	
191	321.44	17.27	2.6 ± 0.1	3.0 ± 0.2	2.6 ± 0.3	···	···	0.1 ± 0.4	PMN J1427-4206	
192	323.74	–24.44	2.0 ± 0.09	1.9 ± 0.1	1.5 ± 0.1	1.7 ± 0.3	···	–0.3 ± 0.3	PMN J1837-7108	
193	325.13	25.60	0.8 ± 0.1	1.7 ± 0.2	1.9 ± 0.2	2.4 ± 0.6	···	1.3 ± 0.6	PMN J1427-3306	*
194	326.21	–34.56	1.0 ± 0.2	1.3 ± 0.2	0.9 ± 0.2	···	2.0 ± 0.7	0.4 ± 0.6	PMN J2035-6846	
195	326.81	–60.81	0.9 ± 0.08	0.8 ± 0.2	···	···	···	–0.6 ± 2	PMN J2336-5236	
196	327.01	–15.87	2.1 ± 0.1	2.0 ± 0.2	1.6 ± 0.2	···	···	–0.3 ± 0.4	PMN J1723-6500	

Table 5—Continued

	l [°]	b [°]	K [Jy]	Ka [Jy]	Q [Jy]	V [Jy]	W [Jy]	α	5 GHz ID
197	327.19	49.19	1.5 ± 0.1	1.2 ± 0.2	2.0 ± 0.4	2.6 ± 0.6	···	0.4 ± 0.5	PMN J1354-1041
198	328.10	–12.44	1.9 ± 0.1	2.0 ± 0.2	2.3 ± 0.2	2.0 ± 0.3	···	0.1 ± 0.3	PMN J1703-6212
199	328.83	–19.57	1.2 ± 0.1	1.4 ± 0.2	1.5 ± 0.2	1.2 ± 0.3	···	0.2 ± 0.5	PMN J1803-6507
200	330.86	–20.79	1.7 ± 0.1	1.2 ± 0.2	1.1 ± 0.2	1.4 ± 0.5	···	-0.7 ± 0.5	PMN J1819-6345
201	331.72	–52.11	1.0 ± 0.07	···	···	···	1.4 ± 0.6	0.2 ± 0.7	PMN J2239-5701
202	332.58	–74.91	1.5 ± 0.1	1.2 ± 0.2	0.9 ± 0.2	1.0 ± 0.3	···	-0.6 ± 0.5	PMN J0013-3954
203	333.90	50.35	1.5 ± 0.2	0.8 ± 0.2	1.5 ± 0.3	···	···	-0.3 ± 0.9	1Jy 1406-076
204	334.81	–60.55	1.2 ± 0.08	1.2 ± 0.1	1.2 ± 0.2	···	···	0.0 ± 0.5	PMN J2315-5018
205	340.68	27.58	1.9 ± 0.1	2.0 ± 0.2	2.0 ± 0.3	1.9 ± 0.6	···	0.1 ± 0.5	PMN J1517-2422
206	344.52	–56.10	2.0 ± 0.1	1.8 ± 0.2	2.0 ± 0.2	2.6 ± 0.4	···	0.1 ± 0.3	PMN J2235-4835
207	351.26	40.16	1.9 ± 0.1	1.9 ± 0.2	1.8 ± 0.3	···	1.7 ± 0.7	-0.1 ± 0.5	1Jy 1510-08
208	352.48	–40.31	1.3 ± 0.1	···	···	1.7 ± 0.5	···	0.2 ± 0.7	PMN J2056-4714

Note. — * indicates the source has multiple possible identifi cations.

9. CONCLUSIONS

1) We have defined and constructed a series of "standard" masks to use for CMB data analyses. The masks vary in degree of the severity of the sky cuts. These masks have been used in the companion *WMAP* papers that analyze the CMB anisotropy.

2) We present a CMB map formed from a weighted combination of the five *WMAP* bands designed to reduce foreground contamination. The method is effective, but care must be used in the use of this map given its complicated noise correlations.

3) We examine the fitting of foreground spatial template maps to the *WMAP* maps to remove foregrounds for CMB analyses. This method can work well as long a mask is applied to exclude the strongest regions of Galactic emission and as long as the fits are restricted in frequency. These restrictions are needed because the foreground tracers are not high fidelity tracers of the *WMAP* forgrounds. A frequency-restricted fit with a mask is used for the current "first year" *WMAP* results.

4) The relatively flat synchrotron spectral index ($\beta \approx -2.5$) in the Galactic plane between 408 MHz and 23 GHz provides evidence for diffusion and convection of cosmic rays within the Galactic plane. The significant steepening of the synchrotron spectral index at high Galactic latitudes suggests that diffusion is the dominant process for cosmic ray electrons leaving the plane, and that these cosmic ray electrons are trapped in the halo for sufficient time to lose a significant amount of their energy.

5) We have made maps and derived spectral indices of the individual physical emission components using a Maximum Entropy Method.

6) The steep spectral index ($\beta \approx -3$) high Galactic latitude features, seen prominantly in low frequency radio maps, become comparatively weaker than the flatter ($\beta \approx -2.5$) synchrotron emission in the plane at the higher *WMAP* frequencies. The consequence of this is that the synchrotron sky map seen by *WMAP* is a much closer tracer of regions of recent star-formation than low radio frequency maps. This, in turn, implies that the spatial distribution of synchrotron emission at the *WMAP* frequencies is strongly correlated with that of other star-formation tracers, such as thermal dust emission. The synchrotron spectral index is steeper in the *WMAP* bands than at radio frequencies.

7) A synchrotron map of the sky is frequency dependent. It is inappropriate to assume that a synchrotron map measured at low frequencies (e.g., 408 MHz) should be a high-fidelity tracer of synchrotron emission at much higher frequencies.

8) The free-free map from *WMAP* is generally consistent with Hα measurements that also trace the ionized gas.

9) The spectral index of the thermal dust emission is steep, $\beta_d \approx 2.2$ in the *WMAP* bands, possibly implying emission from cold silicate grains.

10) There is no frequency at which spinning or magnetic dust emission dominates in the *WMAP* data. Spinning dust emission is < 5 % of the Ka-band antenna temperature.

11) The *WMAP* bands were chosen to be in a region of the spectrum where the ratio of the CMB to foreground contamination was at a maximum. Due to the steep synchrotron and dust spectra, the choice of *WMAP* frequencies was even more advantageous than expected.

12) The total flux of our Galaxy in the five *WMAP* bands is 45, 38, 35, 32, and 48 kJy, from K-band to W-band.

13) The Sunyaev-Zeldovich effect is a negligible "contaminant" for the current first year results, as expected.

14) A catalog of 208 point sources detected by *WMAP* is presented. Of these, five are likely to be spurious.

The mean spectral index of the point sources is $\alpha \sim 0$ ($\beta \sim -2$). Derived source counts suggest a contribution to the anisotropy power of $(15.0 \pm 1.4) \times 10^{-3}\ \mu\mathrm{K}^2\mathrm{sr}$ at Q-band and negligible levels at V-band and W-band.

The *WMAP* mission is made possible by the support of the Office of Space Sciences at NASA Headquarters and by the hard and capable work of scores of scientists, engineers, technicians, machinists, data analysts, budget analysts, managers, administrative staff, and reviewers. The Wisconsin H-Alpha Mapper (WHAM), the Virginia Tech Spectral-Line Survey (VTSS), and the Southern H-Alpha Sky Survey Atlas (SHASSA), are funded by the National Science Foundation. We are grateful to D. Finkbeiner for making his combined Hα map available to us in advance of publication.

REFERENCES

Agladze, N. I., Sievers, A. J., Jones, S. A., Burlitch, J. M., & Beckwith, S. V. W. 1996, ApJ, 462, 1026

Barnes, C., Limon, M., Page, L., Bennett, C., Bradley, S., Halpern, M., Hinshaw, G., Jarosik, N., Jones, W., Kogut, A., Meyer, S., Motrunich, O., Tucker, G., Wilkinson, D., & Wollack, E. 2002, ApJS, 143, 567

Beck, R. & Golla, G. 1988, A&A, 191, L9

Bennett, C. L., Bay, M., Halpern, M., Hinshaw, G., Jackson, C., Jarosik, N., Kogut, A., Limon, M., Meyer, S. S., Page, L., Spergel, D. N., Tucker, G. S., Wilkinson, D. T., Wollack, E., & Wright, E. L. 2003, ApJ, 583, 1

Bennett, C. L., Smoot, G. F., Hinshaw, G., Wright, E. L., Kogut, A., de Amici, G., Meyer, S. S., Weiss, R., Wilkinson, D. T., Gulkis, S., Janssen, M., Boggess, N. W., Cheng, E. S., Hauser, M. G., Kelsall, T., Mather, J. C., Moseley, S. H., Murdock, T. L., & Silverberg, R. F. 1992, ApJ, 396, L7

Bicay, M. D., Helou, G., & Condon, J. J. 1989, ApJ, 338, L53

Biermann, P. 1976, A&A, 53, 295

Bressan, A., Silva, L., & Granato, G. L. 2002, A&A, 392, 377

Chi, X. & Wolfendale, A. W. 1990, MNRAS, 245, 101

Condon, J. J. 1992, ARA&A, 30, 575

de Jong, T., Klein, U., Wielebinski, R., & Wunderlich, E. 1985, A&A, 147, L6

Dennison, B., Simonetti, J. H., & Topasna, G. A. 1998, Publications of the Astronomical Society of Australia, 15, 147

Devereux, N. A. & Eales, S. A. 1989, ApJ, 340, 708

Dickey, J. M. & Salpeter, E. E. 1984, ApJ, 284, 461

Draine, B. T. & Lazarian, A. 1998a, ApJ, 494, L19

—. 1998b, ApJ, 508, 157

—. 1999, ApJ, 512, 740

Dupac, X., Giard, M., Bernard, J.-P., Boudet, N., Lamarre, J.-M., Mény, C., Pajot, F., Pointecouteau, É., Ristorcelli, I., Serra, G., Stepnik, B., & Torre, J.-P. 2002, A&A, 392, 691

Dupac, X., Giard, M., Bernard, J.-P., Lamarre, J.-M., Mény, C., Pajot, F., Ristorcelli, I., Serra, G., & Torre, J.-P. 2001, ApJ, 553, 604

Ebeling, H., Voges, W., Bohringer, H., Edge, A. C., Huchra, J. P., & Briel, U. G. 1996, MNRAS, 281, 799

Erickson, W. C. 1957, ApJ, 126, 480

Finkbeiner, D. P. 2003, ApJS, accepted (astro-ph/0301558)

Finkbeiner, D. P., Davis, M., & Schlegel, D. J. 1999, ApJ, 524, 867

Finkbeiner, D. P., Schlegel, D. J., Frank, C., & Heiles, C. 2002, ApJ, 566, 898

Fitt, A. J., Alexander, P., & Cox, M. J. 1988, MNRAS, 233, 907

Gaustad, J. E., McCullough, P. R., Rosing, W., & Buren, D. V. 2001, PASP, 113, 1326

Gavazzi, G., Cocito, A., & Vettolani, G. 1986, ApJ, 305, L15

Gioia, I. M., Gregorini, L., & Klein, U. 1982, A&A, 116, 164

Green, D. A. 1988, Ap&SS, 148, 3

Green, D. A. & Scheuer, P. A. G. 1992, MNRAS, 258, 833

Gregory, P. C., Scott, W. K., Douglas, K., & Condon, J. J. 1996, ApJS, 103, 427

Griffith, M. R., Wright, A. E., Burke, B. F., & Ekers, R. D. 1994, ApJS, 90, 179

—. 1995, ApJS, 97, 347

Haffner, L. M., Reynolds, R. J., Tufte, S. L., et al. 2002, in preparation

Halverson, N. W., Leitch, E. M., Pryke, C., Kovac, J., Carlstrom, J. E., Holzapfel, W. L., Dragovan, M., Cartwright, J. K., Mason, B. S., Padin, S., Pearson, T. J., Readhead, A. C. S., & Shepherd, M. C. 2002, ApJ, 568, 38

Haslam, C. G. T., Klein, U., Salter, C. J., Stoffel, H., Wilson, W. E., Cleary, M. N., Cooke, D. J., & Thomasson, P. 1981, A&A, 100, 209

Helou, G., Soifer, B. T., & Rowan-Robinson, M. 1985, ApJ, 298, L7

Hinshaw, G. F. et al. 2003, ApJ, submitted

Hirabayashi, H., Fomalont, E. B., Horiuchi, S., Lovell, J. E. J., Moellenbrock, G. A., Inoue, M., Burke, B. F., Dewdney, P. E., Gurvits, L. I., Kobayashi, H., Jauncey, D. L., Murata, Y., McCulloch, P., Preston, R. A., Avruch, I. M., Edwards, P. G., Dougherty, S. M., Scott, W. K., Frey, S., Paragi, Z., Kovalev, Y. A., Popov, M., Romney, J. D., Schilizzi, R. T., Shen, Z., Nicolson, G., Quick, J., Costa, M., Dodson, R., Reynolds, J. E., Tzioumis, A. K., Tingay, S. J., Hong, X., Liang, S., Huang, X., Wei, W., Trigilio, C., Tuccari, G., Nakajima, J., Kawai, E., Umemoto, T., Miyaji, T., Fujisawa, K., Kus, N. K. A., Ghigo, F., Salter, C., Ghosh, T., Kanevsky, B., Slysh, V., Gunn, A., Burgess, P., Carlson, B., Del Rizzo, D., Taylor, R., Cannon, W., Kameno, S., Shibata, K. M., Benson, J., Flatters, C., Hale, A., Lewis, C., Langston, G., Minter, A., Miller, K., Smith, J., Wietfeldt, R., Altunin, V., Meier, D. L., Murphy, D. W., Resch, G., Lister, M. L., Piner, B. G., Jenkins, R., Border, J., & Gimeno, J. 2000, PASJ, 52, 997

Holdaway, M. A., Owen, F. N., & Rupen, M. P. 1994, NRAO report

Hummel, E. 1986, A&A, 160, L4

Hummel, E., Dahlem, M., van der Hulst, J. M., & Sukumar, S. 1991, A&A, 246, 10

Hummel, E., Davies, R. D., Pedlar, A., Wolstencroft, R. D., & van der Hulst, J. M. 1988, A&A, 199, 91

Jarosik, N. et al. 2003, ApJS, 145

Klein, U. & Emerson, D. T. 1981, A&A, 94, 29

Komatsu, E. et al. 2003, ApJ, submitted

Kühr, H., Witzel, A., Pauliny-Toth, I. I. K., & Nauber, U. 1981, A&AS, 45, 367

Landt, H., Padovani, P., Perlman, E. S., Giommi, P., Bignall, H., & Tzioumis, A. 2001, MNRAS, 323, 757

Lawson, K. D., Mayer, C. J., Osborne, J. L., & Parkinson, M. L. 1987, MNRAS, 225, 307

Lisenfeld, U. & Völk, H. J. 2000, A&A, 354, 423

Mason, B. S. et al. 2002, ApJ, submitted (astro-ph/0205384)

Mather, J. C., Fixsen, D. J., Shafer, R. A., Mosier, C., & Wilkinson, D. T. 1999, ApJ, 512, 511

Mennella, V., Brucato, J. R., Colangeli, L., Palumbo, P., Rotundi, A., & Bussoletti, E. 1998, ApJ, 496, 1058

Mirabel, I. F. & Sanders, D. B. 1988, ApJ, 335, 104

Morsi, H. W. & Reich, W. 1987, A&AS, 69, 533

Niklas, S., Klein, U., & Wielebinski, R. 1997, A&A, 322, 19

Oster, L. 1961, Rev Mod Phys, 33, 525

Otte, B., Gallagher, J. S., & Reynolds, R. J. 2002, ApJ, 572, 823

Page, L. et al. 2003a, ApJ, submitted

—. 2003b, ApJ, 585, in press

Park, C., Park, C., & Ratra, B. 2002, ApJ, 568, 9

Perlman, E. S., Padovani, P., Giommi, P., Sambruna, R., Jones, L. R., Tzioumis, A., & Reynolds, J. 1998, AJ, 115, 1253

Press, W. H., Teukolsky, S. A., Vetterling, W. T., & Flannery, B. P. 1992, Numerical Recipes in C, 2nd edn. (Cambridge, UK: Cambridge University Press)

Refregier, A., Spergel, D. N., & Herbig, T. 2000, ApJ, 531, 31

Reich, P. & Reich, W. 1988, A&AS, 74, 7

Reynolds, R. J., Haffner, L. M., & Madsen, G. J. 2002, in ASP Conf. Ser. 282, in press; ed. M. Rosado, L. Binette, L. Arias

Sanders, D. B. & Mirabel, I. F. 1985, ApJ, 298, L31

Saunders, W., Sutherland, W. J., Maddox, S. J., Keeble, O., Oliver, S. J., Rowan-Robinson, M., McMahon, R. G., Efstathiou, G. P., Tadros, H., White, S. D. M., Frenk, C. S., Carramiñana, A., & Hawkins, M. R. S. 2000, MNRAS, 317, 55

Schlegel, D. J., Finkbeiner, D. P., & Davis, M. 1998, ApJ, 500, 525

Schwartz, P. R. 1982, ApJ, 252, 589

Sokasian, A., Gawiser, E., & Smoot, G. F. 2001, ApJ, 562, 88

Stickel, M., Meisenheimer, K., & Kühr, H. 1994, A&AS, 105, 211

Taylor, A. C., Grainge, K., Jones, M. E., Pooley, G. G., Saunders, R. D. E., & Waldram, E. M. 2001, MNRAS, 327, L1

Taylor, A. C. et al. 2002, astro-ph/0205381

Tegmark, M. & de Oliveira-Costa, A. 1998, ApJ, 500, L83

Tegmark, M. & Efstathiou, G. 1996, MNRAS, 281, 1297

Tegmark, M., Eisenstein, D. J., Hu, W., & de Oliveira-Costa, A. 2000, ApJ, 530, 133, astro-ps/9905257

Teräsranta, H., Urpo, S., Wiren, S., & Valtonen, M. 2001, A&A, 368, 431

Toffolatti, L., Argueso Gomez, F., de Zotti, G., Mazzei, P., Franceschini, A., Danese, L., & Burigana, C. 1998, MNRAS, 297, 117

Ulvestad, J. S. 1982, ApJ, 259, 96

Unger, S. W., Wolstencroft, R. D., Pedlar, A., Savage, A., Clowes, R. G., Leggett, S. K., & Parker, Q. A. 1989, MNRAS, 236, 425

Voelk, H. J. 1989, A&A, 218, 67

Wright, A. E., Griffith, M. R., Burke, B. F., & Ekers, R. D. 1994, ApJS, 91, 111

Wright, A. E., Griffith, M. R., Hunt, A. J., Troup, E., Burke, B. F., & Ekers, R. D. 1996, ApJS, 103, 145

Wunderlich, E. & Klein, U. 1988, A&A, 206, 47

—. 1991, A&AS, 87, 247

Wunderlich, E., Wielebinski, R., & Klein, U. 1987, A&AS, 69, 487

This preprint was prepared with the AAS LaTeX macros v5.0.